# A novel function for the MAP kinase SMA-5 in intestinal tube stability

Florian Geisler[a,†], Harald Gerhardus[a,†], Katrin Carberry[a], Wayne Davis[b], Erik Jorgensen[b], Christine Richardson[c], Olaf Bossinger[a,‡,§,*], and Rudolf E. Leube[a,‡,*]

[a]Institute of Molecular and Cellular Anatomy, RWTH Aachen University, 52074 Aachen, Germany; [b]Department of Biology and Howard Hughes Medical Institute, University of Utah, Salt Lake City, UT 84112-0840; [c]School of Biological and Biomedical Sciences, Durham University, Durham DH1 3LE, United Kingdom

**ABSTRACT** **Intermediate filaments are major cytoskeletal components whose assembly into complex networks and isotype-specific functions are still largely unknown. *Caenorhabditis elegans* provides an excellent model system to study intermediate filament organization and function in vivo. Its intestinal intermediate filaments localize exclusively to the endotube, a circumferential sheet just below the actin-based terminal web. A genetic screen for defects in the organization of intermediate filaments identified a mutation in the catalytic domain of the MAP kinase 7 orthologue *sma-5(kc1)*. In *sma-5(kc1)* mutants, pockets of lumen penetrate the cytoplasm of the intestinal cells. These membrane hernias increase over time without affecting epithelial integrity and polarity. A more pronounced phenotype was observed in the deletion allele *sma-5(n678)* and in intestine-specific *sma-5(RNAi)*. Besides reduced body length, an increased time of development, reduced brood size, and reduced life span were observed in the mutants, indicating compromised food uptake. Ultrastructural analyses revealed that the luminal pockets include the subapical cytoskeleton and coincide with local thinning and gaps in the endotube that are often enlarged in other regions. Increased intermediate filament phosphorylation was detected by two-dimensional immunoblotting, suggesting that loss of SMA-5 function leads to reduced intestinal tube stability due to altered intermediate filament network phosphorylation.**

**Monitoring Editor**
Jeffrey D. Hardin
University of Wisconsin

Received: Feb 17, 2016
Revised: Sep 26, 2016
Accepted: Oct 5, 2016

## INTRODUCTION

Intermediate filaments, actin filaments, and microtubules are the main components of the metazoan cytoskeleton and are involved in most cellular processes. The contribution and properties of the three components differ, however. The least investigated elements are the molecularly highly diverse intermediate filaments. In contrast to actin filaments and microtubules, they are not essential for either cell division or basic cell functions. Yet mutations in intermediate filament genes have been implicated in more than 80 human diseases (Omary, 2009).

Intermediate filaments have unique mechanical properties. They are highly flexible and extensible but support, at the same time, cellular stiffness (Stamenovic and Wang, 2000; Ramms *et al.*, 2013; Seltmann *et al.*, 2013; Mendez *et al.*, 2014). Their contribution to mechanical stress resilience is reflected by the large number of blister-forming diseases that are caused by single-point mutations of epithelial keratin intermediate filament–encoding genes (Homberg *et al.*, 2015). Besides these mechanical functions, intermediate filaments are involved in the regulation of cell growth, apoptosis, and vesicle trafficking to name but a few other functions (Kim and Coulombe, 2007; Magin *et al.*, 2007; Toivola *et al.*, 2010). To facilitate these functions, intermediate filaments form complex three-dimensional networks whose arrangement depends on the cell type, cell cycle stage, and functional state.

This article was published online ahead of print in MBoC in Press (http://www.molbiolcell.org/cgi/doi/10.1091/mbc.E16-02-0099) on October 12, 2016.

†These authors contributed equally to this work.

‡These authors contributed equally to this work.

§Present address: Institute of Anatomy I, Molecular Cell Biology, University of Cologne, 50937 Cologne, Germany.

*Address correspondence to: Rudolf E. Leube (rleube@ukaachen.de) and Olaf Bossinger (olaf.bossinger@uk-koeln.de).

Abbreviations used: BLAST, Basic Local Alignment Search Tool; CGC, *Caenorhabditis* Genetics Center; DSS, dextran sodium sulfate; DTT, dithiothreitol; IgG, immunoglobulin G; IL-6, interleukin-6; IPTG, isopropyl β-D-1-thiogalactopyranoside; RNAi, RNA interference; UTR, untranslated region.



Supplemental Material can be found at:
http://www.molbiolcell.org/content/suppl/2016/10/10/mbc.E16-02-0099v1.DC1.html

A particularly striking arrangement of the intermediate filament cytoskeleton is encountered in intestinal epithelial cells. The bulk of intermediate filaments is concentrated in a dense fibrous layer just below the apical terminal web of actin and spectrin in these cells. These layers are anchored to the apical junctional complex in vertebrates including fish (Markl and Franke, 1988), amphibians (Maurizii *et al.*, 2000), and mammals (Iwatsuki and Suda, 2010). This remarkable distribution is also conserved in the nematode *Caenorhabditis elegans*, in which intermediate filaments localize to the prominent endotube (Bossinger *et al.*, 2004; Carberry *et al.*, 2009; Coch and Leube, 2016). It has been also observed in the basal hexapod *Isotumurus maculatus*, which—in contrast to other hexapods—expresses cytoplasmic intermediate filaments (Mencarelli *et al.*, 2011). Taken together, these findings indicate it is likely that the highly conserved distribution pattern is advantageous to intestinal cells and suggests that it strengthens the mucosal barrier function (Geisler and Leube, 2016).

The intermediate filament–rich subapical network might form an intracellular barrier to the cytoplasmic space beneath and is closely attached to the organelle-free terminal web above, which serves as an anchor for the actin bundles that protrude into the microvilli of the overlying brush border (Hirokawa *et al.*, 1982). The terminal web contains myosins, spectrins, actin, and an assortment of actin-binding proteins (see reviews in Mooseker, 1985; Fath and Burgess, 1995; Ku *et al.*, 1999; Thomas, 2001). Assembly of the terminal web has been studied during gut development in vertebrates (Chambers and Grey, 1979), but its relationship to the intermediate filament network is still largely unexplored.

To identify structural determinants and regulatory components of the intestinal cytoskeleton and to study its functional contribution to intestinal physiology, we performed a mutagenesis screen using a reporter strain producing cyan fluorescent protein (CFP)-tagged intermediate filament protein IFB-2::CFP exclusively in the intestinal endotube (Hüsken *et al.*, 2008). Using this strategy, we recently identified the novel intestinal filament organizer IFO-1, which acts as a structural component to localize the intermediate filament–rich endotube to the periluminal subapical cytoplasmic region of intestinal cells (Carberry *et al.*, 2012). Here we characterize mutants of the MAP kinase 7 orthologue SMA-5, which has been linked to growth regulation (Watanabe *et al.*, 2005), and show that *sma-5* alleles induce the development of bubble-shaped invaginations of the apical plasma membrane together with the associated actin and modified intermediate filament cytoskeleton into the cytoplasm of intestinal cells.

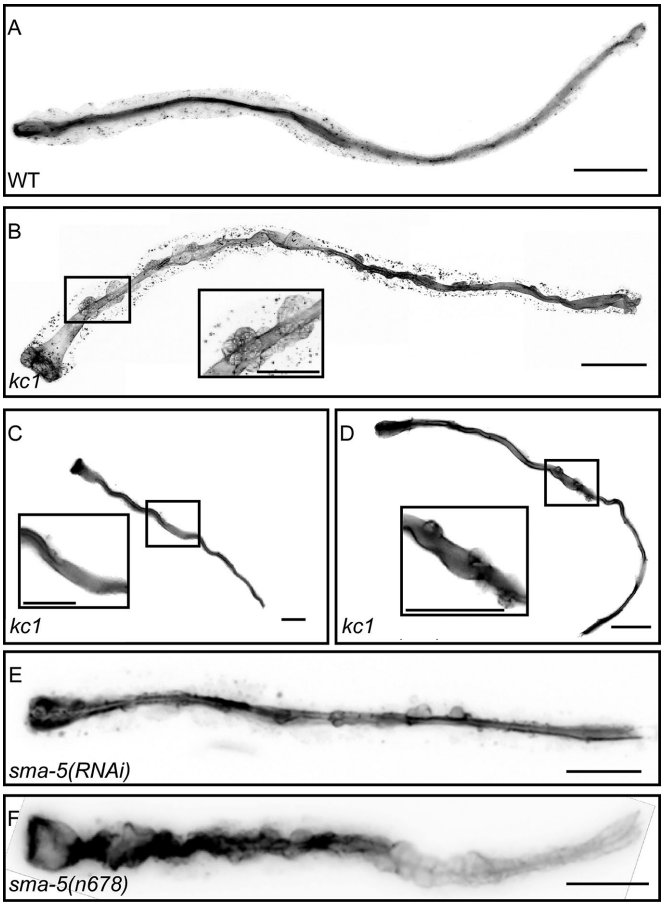


FIGURE 1: Mutations in the *sma-5* gene induce bubble-shaped protrusions of IFB-2::CFP into the cytoplasm of intestinal cells. The fluorescence images (inverse presentation; composite images in B, E, and F) show IFB-2::CFP distribution. Note the smooth and even periluminal localization of IFB-2::CFP in the adult wild-type background (WT; strain BJ52; A), while multiple protrusions along the entire intestine are readily detectable in the adult *kc1* mutant (B). Note also that the *kc1* L1 larva in C is still devoid of invaginations and that the young adult in D presents some invaginations but not as many as the older adult in B. Enlargements correspond to boxed areas. (E, F) Similar multiple cytoplasmic invaginations of IFB-2 are also present in worms treated with *sma-5(RNAi)* and in mutants carrying a partial deletion of the *sma-5* gene (allele *n678*). Scale bars: 100 µm in A, B, D, E, F, and inset in D; 50 µm in inset of B; 10 µm in C and inset in C.

## RESULTS

### SMA-5 mutations induce IFB-2::CFP–labeled cytoplasmic invaginations in the intestine

Allele *kc1* was selected in a mutagenesis screen of IFB-2::CFP–expressing strain BJ52 (details in Carberry *et al.*, 2012). Fluorescence microscopy of outcrossed homozygous strain BJ132 revealed that the circumferential localization of the IFB-2–labeled endotube was disrupted presenting multiple bubble-shaped IFB-2::CFP–positive protrusions into the apical cytoplasm along the entire length of the adluminal surface of all intestinal epithelial cells (Figure 1, A and B). These alterations were not detectable during embryogenesis (unpublished data) and larval development (Figure 1C) but emerged from early adulthood onward (Figure 1D), increasing in number throughout the intestine during aging (Figures 1B and 2, B, E, and H).

We used chromosomal and subchromosomal single-nucleotide polymorphism mapping to localize the *kc1* mutation to the interval between 6.6 and 6.97 cM on the X chromosome, a region encompassing 94 protein-coding genes. The *kc1*-like phenotype was then mapped by bacterial feeding and microinjection of dsRNA to the *sma-5* gene W06B3.2 (Figure 1E), which had been recently characterized by Watanabe and colleagues (2005). They showed that its mutation (allele *n678*) causes small body size despite unaltered cell numbers, slow growth, and abnormal intestinal granules. Aberrations of the intestinal cytoskeleton, however, were not investigated in this study. We therefore crossed the *sma-5(n678)* allele into the *ifb-2::cfp* reporter background. The resulting worms presented an even more severe phenotype of IFB-2::CFP distribution than those carrying the *sma-5(kc1)* allele, with many more invaginations in adults and already detectable invaginations in early larval stages (Figures 1F and 2, C, F, and I).

To demonstrate that a lack of functional SMA-5 is responsible for the *kc1* phenotype, we performed rescue experiments with a fosmid construct that we obtained from the TransgeneOme Project

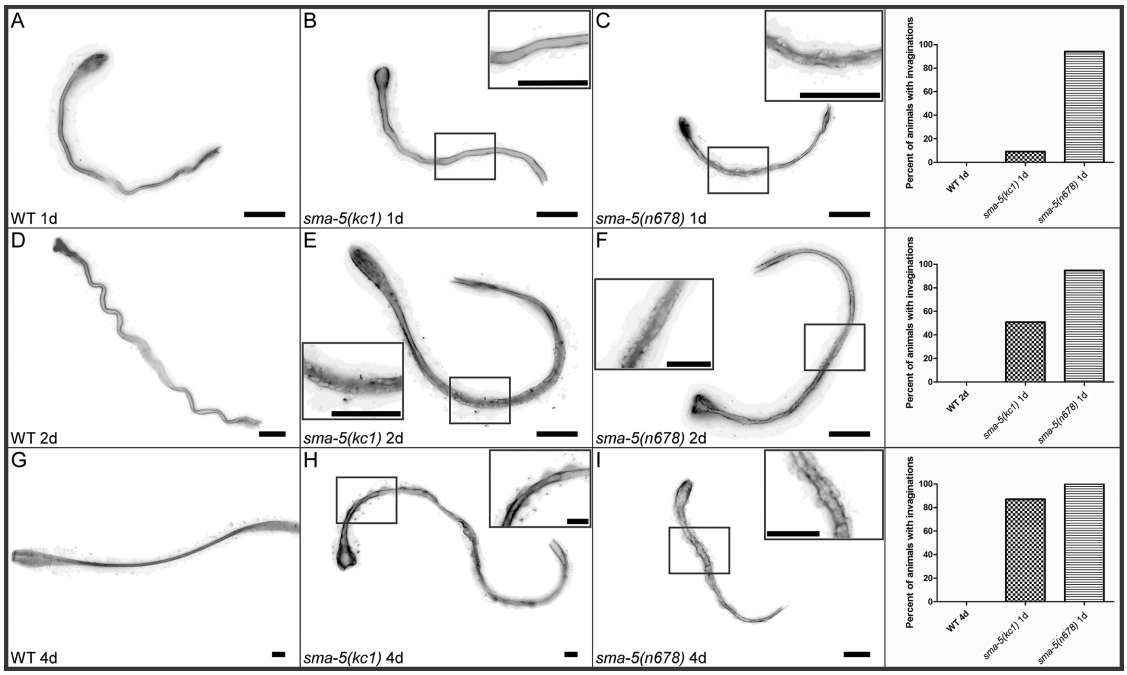


FIGURE 2: Development of the *sma-5* phenotype is age-dependent. IFB-2::CFP fluorescence (inverse presentation) was recorded 1 d (A–C), 2 d (D–F), and 4 d (G–I) after hatching. The percentage of animals showing a cytoplasmic invagination phenotype is shown at right. Wild-type animals were completely devoid of invaginations at all time points (A, D, G; 1 d: 0% [$n = 0/16$]; 2 d: 0% [$n = 0/13$]; 4 d: 0% [$n = 0/21$]), while a few *sma-5(kc1)* animals displayed scarce invaginations at 1 d (B; 9.10% [$n = 2/22$]). A substantial increase in number of affected animals and density of cytoplasmic invaginations occurred during aging (E, H; 2 d: 50.82% [$n = 31/61$]; 4 d: 87.04% [$n = 47/54$]). Most animals carrying allele *n678* presented cytoplasmic invaginations already 1 d after hatching (C; 94.12% [$n = 16/17$]) and 2 d after hatching (F; 2 d: 94.74% [$n = 18/19$]), leading to full penetrance by 4 d after hatching (I; 4 d: 100% [$n = 28/28$]). Scale bars: 20 µm in A–I; 10 µm in inset of F; 20 µm in all other insets.

(https://transgeneome.mpi-cbg.de/transgeneomics/index.html). This construct encodes the SMA-5–enhanced green fluorescent protein (EGFP) fusion protein SMA-5::EGFP. Microinjection of fosmid DNA into the gonads of *sma-5(kc1)* and *sma-5(n678)* animals efficiently rescued the bubble-shaped invaginations observed in matched control animals (Figure 3, A–B″). Similarly, intestine-specific expression of SMA-5 using the *vha-6* promoter (Oka *et al.*, 2001) also rescued the phenotype (Figure 3, C–D′). Furthermore, the SMA-5::EGFP fluorescence was exclusively detected in the cytoplasm of intestinal cells in strain BJ269 (Figure 3, B′ and B″). This was somewhat in contrast to the previous observations of Watanabe *et al.* (2005), who found expression of two *sma-5* reporter constructs, which contain 1.6 kb of the upstream region and either almost none or all of the gene-coding region, not only in the intestine but also in the excretory cell and to some degree in the hypodermis. In addition, our observations were in disagreement with the distribution of another reporter containing 4.9 kb of the region upstream of exon 1 described by the same group, the expression of which was noted only in the pharynx and hypodermis. To exclude that the *kc1* background is responsible for the observed differences, we also injected fosmid DNA into strain DP38 *unc-119(ed3)* leading to progeny expressing the wild-type copy of *unc-119* together with the *sma-5::egfp* transgene. Fluorescence analyses of resulting non-*unc* strain BJ263 again showed intestine-restricted cytoplasmic expression of the fluorescent reporter with no detectable fluorescence in the pharynx, hypodermis, or excretory cell (Figure 4). A localized dot-like signal was seen in the somatic gonad in situ and in dissected worms when using anti-GFP antibodies after long exposure times (Figure 4, D′, E′, and F′). Of note, SMA-5::EGFP fluorescence intensity was highest at the apical pole of intestinal cells (Figure 4B′). To further assess whether SMA-5 function for intermediate filament organization is restricted to the intestine, we investigated the effect of *sma-5(RNAi)* on IFA-1 distribution in the marginal cells of the pharynx and of IFB-1 distribution in the hypodermis. In contrast to IFB-2, these intermediate filaments remained properly arranged upon SMA-5 depletion (Supplemental Figure S1; compare with wild-type distribution in Karabinos *et al.*, 2003; Woo *et al.*, 2004).

### *sma-5(kc1)* carries a point mutation in the region encoding a highly conserved catalytic serine–threonine kinase domain

The WormBase gene model (www.wormbase.org) of the *sma-5* gene predicts four protein isoforms: a, b, c, and d. They give rise to polypeptides with a molecular weight of 56.7 kDa (a), 55 kDa (b), 57.6 kDa (c), and 51.3 kDa (d) and isoelectric points of 7.4, 6.61, 6.71, or 6.94, respectively. Further analysis based on RNAseq data suggests the appearance of alternative splice variants of isoform c (c1 and c2) and isoform d (d1 and d2) (Supplemental Figure S2). Of note, the cDNA corresponding to isoform a was used to successfully rescue the intestinal phenotype using the *vha-6* promoter (Figure 3, D and D′).

A BLAST (Basic Local Alignment Search Tool) search revealed that SMA-5 orthologues are present in other nematodes including *Caenorhabditis remanei*, *Caenorhabditis japonica*, *Caenorhabditis briggsae*, *Pristionchus pacificus*, and *Caenorhabditis brenneri* with amino acid similarities of 99.2, 98.2, 94.9, 78.2, and 77.4%, respectively. More importantly, searches in the KEGG database (www.genome.jp/kegg) showed that SMA-5 orthologues are conserved throughout the

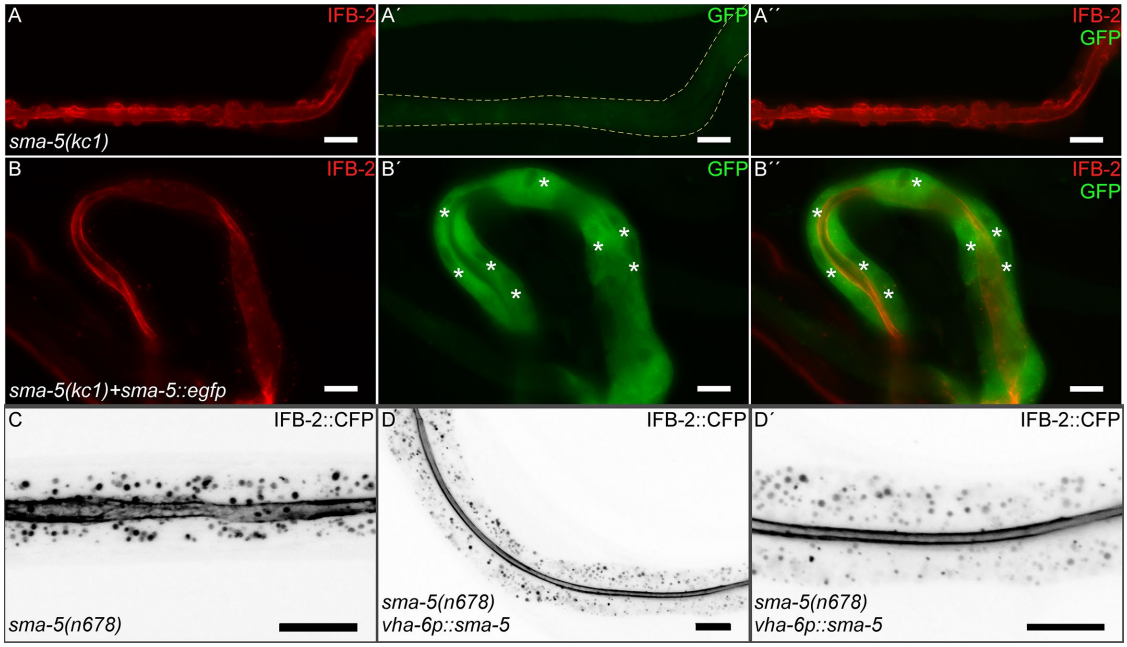


FIGURE 3: The *sma-5* phenotype can be fully rescued by *sma-5::egfp* and intestine-specific *vha-6p::sma-5* expression. (A–B″) The images show immunofluorescence micrographs of dissected adult intestines depicting the staining of anti–IFB-2 (A, B) and anti-GFP delineating the distribution of SMA-5::EGFP (A′, B′; merged images in A″ and B″) in *sma-5(kc1)* animals (A–A″) and in *sma-5(kc1)* animals producing a SMA-5::EGFP fusion protein (B–B″). Note the disappearance of the multiple cytoplasmic invaginations of the IFB-2 network in the rescued intestine. The pancytoplasmic localization of SMA-5::EGFP in the intestine can be appreciated in B′ and B″ (nuclei devoid of fluorescence marked by asterisks). The outline of the intestine is demarcated by broken lines in A′. (C–D′) Fluorescence micrographs (inverse presentation) of living worms depicting the distribution of IFB-2::CFP in *sma-5(n678)* animals (C) and in *sma-5* animals microinjected with the intestine-specific expression construct *vha-6p::sma-5* (strain BJ301; low and high magnification in D and D′, respectively). Note the efficient rescue of the intestinal cytoplasmic invagination phenotype in the microinjected worm. Scale bars: 20 μm.

animal kingdom, including in the model organisms *Drosophila melanogaster* and *Danio rerio* (Supplemental Figure S3). The human SMA-5 orthologue still shows a similarity of 36% to the nematode counterpart. It encodes the 816 amino acid isoform 1 of mitogen-activated protein kinase 7 (BMK1/ERK5; ENSP00000311005).

Sequencing the entire *sma-5* gene of *kc1* animals showed that the gene contains a single point mutation (position 998 in CELE_W06B3.2a) resulting in a change of $R_{125}$ (CGC) into $H_{125}$ (CAC) (marked in yellow in Supplemental Figure S3). Protein domain analysis using the SMART-server (http://smart.embl-heidelberg.de) identified SMA-5 as a serine–threonine kinase with a typical catalytic domain located between amino acids 81 and 388 in isoform a. Remarkably, $R_{125}$ is contained in a highly conserved sequence motif, which shows similarities to *D. melanogaster* (38.5%), *D. rerio* (40.4%), and *Homo sapiens* (42.3%). $R_{125}$ is just three amino acids away from one of the essential and also fully conserved amino acids ($E_{129}$; marked in blue in Supplemental Figure S3). This can be taken as an indication for dysfunctional kinase activity of the *kc1*-encoded SMA-5 mutant protein. In contrast, the *sma-5(n678)* allele contains a 226 base pair deletion of the 3′ coding region of *sma-5*, leading to truncation of the last 75 amino acids in addition to a complete ~15 kb deletion of the downstream genes C49F5.3, C49F5.5, C49F5.6, and C49F5.7 (Watanabe *et al.*, 2005).

### *sma-5* mutants are small and have reduced brood size, slower larval development, and decreased life span

Next we wanted to investigate the consequences of the altered intestine for worm growth, replication, development, and survival. The histogram in Figure 5A shows that *sma-5(kc1)* worms were smaller (1.11 ± 0.05 mm; $n = 38$) than the wild type (1.27 ± 0.06 mm; $n = 54$; $p < 0.001$) and that *sma-5(n678)* worms were even smaller (0.72 ± 0.10 mm; $n = 37$; $p < 0.001$). Furthermore, the number of progeny was significantly ($p < 0.001$) less in *sma-5(kc1)* (168 ± 29; $n = 40$) and *sma-5(n678)* (69 ± 22; $n = 44$) than in the wild type (209 ± 21; $n = 50$; Figure 5B). Increased embryonic lethality was not observed in the mutants (unpublished data), but development was considerably ($p < 0.001$) prolonged in the mutants (Figure 5C). Time of development at 18°C was 5.01 ± 0.11 d in the wild type ($n = 265$), 5.59 ± 0.49 d in *sma-5(kc1)* ($n = 269$), and 7.36 ± 0.65 d in *sma-5(n678)* ($n = 181$). In addition, a reduced life span was observed in both *sma-5* alleles (*kc1*: 19 d; $n = 468$; *n678*: 17 d; $n = 461$) versus the wild type (25 d; $n = 512$; $p < 0.001$) (Figure 5D).

To demonstrate that the phenotype was caused by intestine-specific loss of SMA-5 function, we performed *sma-5(RNAi)* experiments in strain OLB11, which facilitates selective RNA interference (RNAi) in the intestine (Pilipiuk *et al.*, 2009). These animals not only replicated the characteristic cytoplasmic invaginations in the intestine but also showed reduced growth, retarded development, and reduced brood size (Supplemental Figure S4). Conversely, SMA-5::EGFP expression in *n678* mutants not only rescued the intestinal phenotype but also rescued body size (935.0 ± 10.42 μm; $n = 46$ in rescued worms vs. 1035 ± 14.63 μm; $n = 41$ in wild type and 603.4 ± 15.99 μm; $n = 47$ in *n678* mutants; $p < 0.0001$). Taken together, the observed phenotypes are indicative of compromised food resorption.

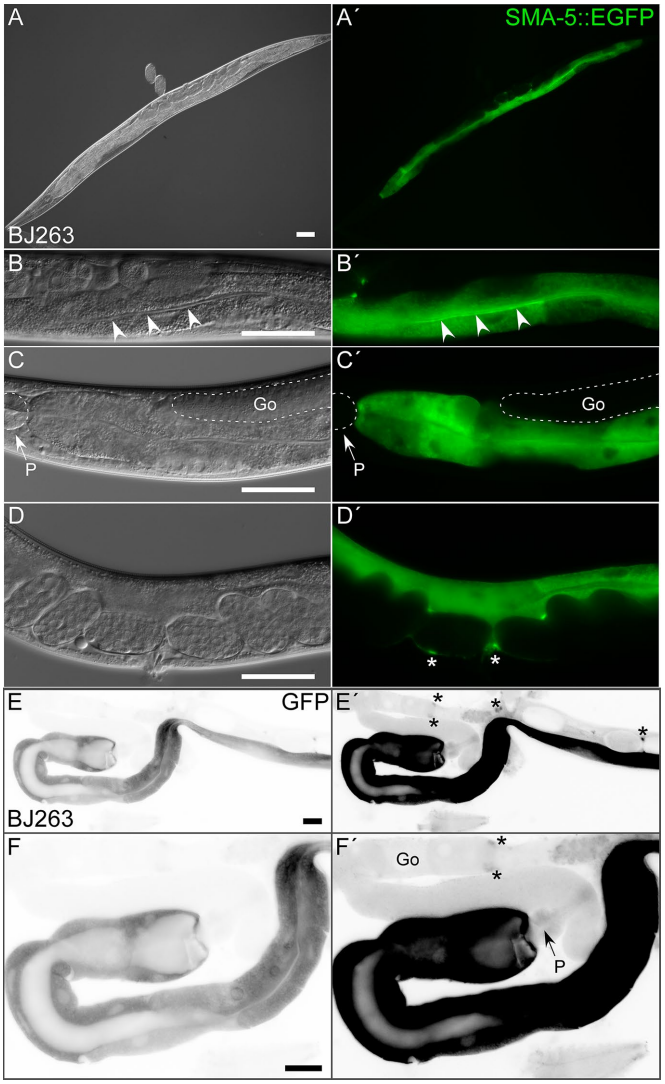


FIGURE 4: SMA-5::EGFP is detected throughout the entire intestine and weakly in restricted regions of the somatic gonad. The in vivo fluorescence pictures in A′–D′ (corresponding interference contrast images in A–D) and immunofluorescence pictures of dissected intestines detecting GFP (E–F′) show expression of an extrachromosomal *sma-5::egfp*–containing fosmid. Note that the fluorescence is restricted to the cytoplasm of enterocytes, with prominent apical enrichment in some instances (arrowheads in B) with no detectable expression in either pharynx (P) or gonad (Go) even after overexposure (E′ and F′). Occasionally, localized expression was noted in the somatic gonad (asterisks in D′, E′, and F′) Scale bars: 50 µm in A–D′; 25 µm in E–F′.

### *sma-5* mutations induce an overall reorganization of the apical cytoskeleton in the intestine but do not perturb junction localization and integrity

Differential interference contrast microscopy revealed that the bubble-shaped structures bulged out from the intestinal lumen (arrows in Figure 6, B–D). These invaginations were much more frequent and pronounced in *n678* than in *kc1* mutants. The adjacent apical domain, however, was still inconspicuous (arrowheads in Figure 6, B–D). Luminal width was often enlarged, especially in *n678* mutants (asterisks in Figure 6D). To find out whether these invaginations are connected to the intestinal lumen and whether they are surrounded by IFB-2, we performed feeding experiments with the membrane-impermeable dye Texas Red-dextran in IFB-2::CFP reporter strains ($n$ = 50). The dye was restricted to the intestinal lumen in wild-type and mutant worms, demonstrating that the intestinal barrier remains intact. In addition, the dye filled all the luminal pockets that herniate into the cytoplasm in the *kc1* ($n$ = 50) and *n678* mutants ($n$ = 50; Figure 6, E–G″). These cytoplasmic invaginations were surrounded by IFB-2::CFP fluorescence, which often appeared to be discontinuous.

To examine the structural and topological integrity of the *C. elegans* apical junction (CeAJ), we performed immunofluorescence microscopy on isolated adult intestines with antibodies directed against the junctional MAGUK protein DLG-1 (Figure 7, A″–C″). The localization and continuity of immunostaining was unperturbed in the mutants presenting the characteristic ladder pattern. This result further supports the dextran-feeding experiments demonstrating that the intestinal barrier function is still fully intact. Next we wanted to study the effect of *sma-5* mutation on other intermediate filament polypeptides in the intestine. Figure 7, A–C′, shows that IFC-2 perfectly colocalizes with IFB-2 in both the wild-type and mutant intestines. To test, whether and how other components of the apical cytoskeleton are affected, we studied the distribution of F-actin. As expected, phalloidin staining showed apical F-actin enrichment next to IFB-2 immunoreactivity (e.g., Carberry *et al.*, 2012). This codistribution was maintained in the mutants with F-actin staining in the IFB-2–positive cytoplasmic invaginations (Figure 7, D–F″). In the following set of experiments, we looked at the cytoskeletal linker ezrin–radixin–moesin *C. elegans* orthologue ERM-1, which links actin to the plasma membrane (Göbel *et al.*, 2004; van Fürden *et al.*, 2004; Fievet *et al.*, 2007; Fehon *et al.*, 2010). As exemplified in Figure 7, H–I″, ERM-1 also localizes to the cytoplasmic invaginations of both *sma-5* mutants. Taking these findings together, we conclude that the entire apical membrane domain is displaced into the cytoplasm of *sma-5* mutants, and these invaginations remain in direct contact with the intestinal lumen.

### The intestinal filament organizer IFO-1 acts additively with SMA-5

Because the recently characterized intestinal filament organizer IFO-1 plays a crucial role in correct localization of the subapical intermediate filament and actin cytoskeleton in the intestine (Carberry *et al.*, 2012), we examined the distribution of IFO-1 in the *sma-5* mutant background. As expected, IFO-1 codistributed closely with IFB-2 in the subapical intestinal cytoplasm (Figure 8, A–A″). It also codistributed in mature invaginations of *sma-5(RNAi)*-treated animals (Figure 8, B–B″). Slight differences between IFO-1 and IFB-2 distribution were, however, occasionally detectable, especially in smaller invaginations, where strong IFO-1 fluorescence was detectable without significant IFB-2 (Figure 8, B–B″ and Supplemental Figure S5). The findings indicate either that IFO-1 precedes cytoplasmic translocation of IFB-2 or that cytoplasmic invaginations occur at positions of a discontinuous, that is incomplete, IFB-2 network.

To further investigate the genetic relationship between *sma-5* and *ifo-1*, we prepared double knockdowns. Supplemental Figure S6 shows that *ifo-1(RNAi)* in *sma-5(kc1)* induced both the *sma-5*–dependent cytoplasmic invaginations and the enrichment of IFB-2 at the CeAJ that is typically found in *ifo-1* mutants. Junctional integrity remained intact, and no additional phenotype was detected. The additive nature of the phenotype indicates that the mutations act on intermediate filament network organization at least in part through separate pathways.

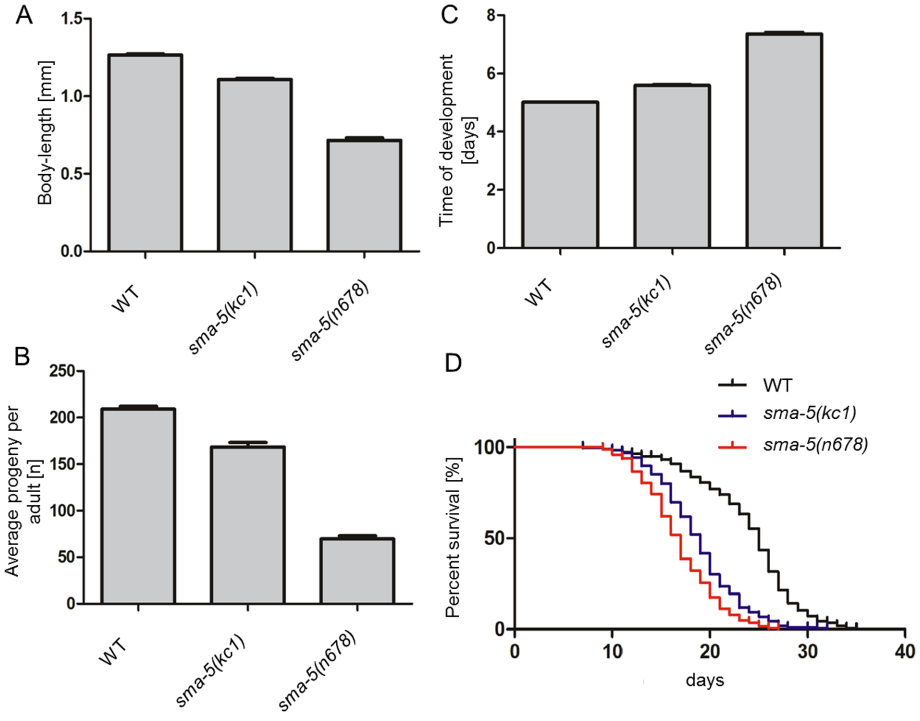


FIGURE 5: *sma-5* mutations lead to impaired growth, reduced brood size, slowed development, and decreased survival. (A) The histogram shows that *sma-5(kc1)* and *sma-5(n678)* worms are smaller (1.11 ± 0.05 mm [$n = 38$] and 0.72 ± 0.10 mm [$n = 37$], respectively) than the wild type (1.27 ± 0.06 mm; $n = 54$; $p < 0.001$). (B) The number of progeny is significantly ($p < 0.001$) smaller in *sma-5(kc1)* (168 ± 29; $n = 40$) and *sma-5(n678)* (69 ± 22; $n = 44$) than in the wild type (209 ± 21; $n = 50$). (C) The time of development at 18°C is considerably ($p < 0.001$) prolonged in *sma-5(kc1)* (5.59 ± 0.49 d; $n = 269$) and *sma-5(n678)* (7.36 ± 0.65 d; $n = 181$) compared with the wild type (5.01 ± 0.11 d; $n = 265$). (D) Life span is considerably reduced in both *sma-5* alleles (*kc1*: 19 d [$n = 468$]; *n678*: 17 d [$n = 461$]) vs. the wild type (25 d; $n = 512$; $p < 0.001$).

### SMA-5 is needed for structural maintenance of the intermediate filament–rich endotube and ordered arrangement of microvilli

Electron microscopy was performed to study luminal alterations at the ultrastructural level. In the wild-type situation ($n = 3$), the intestinal lumen, in transverse section, has a regular ellipsoid shape and is surrounded by evenly sized and regularly arranged microvilli of the brush border (Figure 9, A–C; see also Carberry *et al.*, 2012; www.wormatlas.org). The intermediate filament–rich endotube appears as an electron-dense structure surrounding the lumen below the organelle-free terminal web (green arrowheads). It is anchored to the CeAJ at cell–cell borders (white arrowheads). When viewed in longitudinal section, *kc1* and *n678* mutants (Figure 9, D–I; $n = 4$ for *kc1*; and $n = 4$ for *n678*) showed luminal pockets extending into the intestinal cytoplasm that were not observed in the wild type. The invaginations were still connected to the intestinal lumen, and no additional lumina were observed. These pockets are formed at transition zones where the endotube is considerably thinned (yellow arrowheads) or completely missing (red arrowheads). Overall local endotube thinning was observed in both mutant backgrounds, although it was more pronounced and combined with much larger gaps in *n678*. Local endotube thickening was not seen in *kc1* but was quite pronounced in *n678* (blue arrowheads). Taken together, these findings indicate that the continuity of the endotube is compromised in the mutant intestine, leading to cytoplasmic invaginations, and likely explains the reduced/absent decoration by IFB-2 (Figure 8, B–B″, and Supplemental Figure S5). Furthermore, the regular microvillar arrangement was considerably perturbed in several regions (e.g., Figure 9, I and L). Regular spacing and orthogonal protrusion of microvilli, which are so characteristic for a genuine brush border, were lost. Finally, the CeAJs were morphologically inconspicuous, supporting the observed functional integrity of the intestinal barrier (Figure 9, J–L).

### SMA-5 activity affects phosphorylation of intermediate filament proteins

To test whether the observed structural alterations of the IF system are linked to altered phosphorylation of intermediate filament polypeptides, we performed two-dimensional gel electrophoresis and immunoblotting to detect changes in isoelectric points. Figure 10 shows results using anti–IFB-2 antibodies. In wild-type N2, a single isoelectric variant could be detected for the higher molecular weight isoform IFB-2a, while two isoelectric variants were visible for the lower molecular weight isoform IFB-2c with a major spot (2c and $2c^{+1P}$, respectively). Phosphatase treatment resulted in a shift of isoelectric points toward basic with the appearance of new immunoreactive signals labeled as $2a^{-1P}$ and $2c^{-1P}$. A different pattern of IFB-2 immunoreactivity was observed in lysates obtained from *sma-5(n678)* worms with an overall reduction of isoelectric points and appearance of new signals in the more acidic part of the pH gradient ($2a^{+1P}$, $2a^{+2P}$, $2c^{+2P}$). Phosphatase treatment reversed this pattern toward more basic isoelectric variants. These data support the notion that intermediate filament polypeptides are phosphorylated and indicate that SMA-5 inactivation leads to increased intermediate filament phosphorylation. To examine whether this paradoxical effect might be mediated through altered ERM-1 phosphorylation, we performed immunoblots (Supplemental Figure S7). They show that the overall ERM-1 expression is reduced, while the fraction of phosphorylated ERM-1 remains unaltered in *n678* mutants.

## DISCUSSION

We provide genetic evidence that kinase activity is linked to intermediate filament network stability in the polarized simple epithelium of the *C. elegans* intestine by identifying the serine–threonine MAPK7 kinase orthologue SMA-5 as a key regulator of intermediate filament network organization. In *sma-5* mutants, the intermediate filament protein IFB-2 is hyperphosphorylated rather than hypophosphorylated, as one might expect if IFB-2 was a direct target of SMA-5. Therefore it is more likely that SMA-5 activates another kinase or inhibits a phosphatase that could then act on intermediate filaments. We describe phenotypic changes in the two mutant *sma-5* alleles, *n678* and *kc1*. The more severe phenotype in *n678* mutants is caused by a carboxy-terminal deletion of 75 amino acids, presumably yielding a nonfunctional polypeptide, while the much milder phenotype in *kc1* mutants is linked to a mutation in a single conserved residue within the catalytic domain that may render the encoded enzyme less active but not completely dysfunctional.

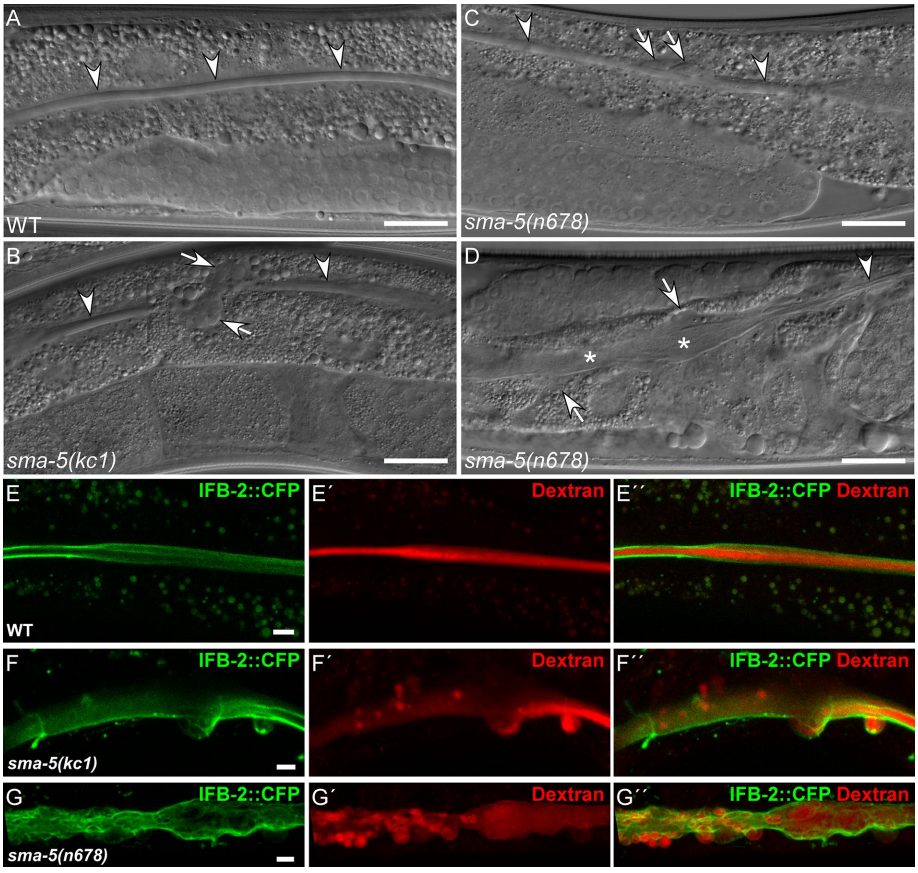


FIGURE 6: *sma-5* mutations induce cytoplasmic IFB-2–positive invaginations connected to the intestinal lumen that is often dilated. (A–D) The differential interference contrast microscopic images depict the characteristic even-shaped lumen (arrowheads) in wild-type N2 (WT; A), while multiple cytoplasmic invaginations (arrows) and local luminal expansions (asterisks) occur in *sma-5(kc1)* and *sma-5(n678)* mutants next to normal-appearing sections (arrowheads; B–D). (E–G″) Fluorescence micrographs detect IFB-2::CFP and Texas Red–labeled dextran after feeding in wild-type (E–E″; $n = 50$), *sma-5(kc1)* (F–F″; $n = 50$), and *sma-5(n678)* (G–G″; $n = 50$) intestines. Note that the membrane-impermeable dye is restricted to the even-shaped lumen in the wild type but enters bubble-shaped protrusions that are surrounded by cytoplasmic IFB-2::CFP in both mutants. The intestinal barrier remains intact in the mutants. Scale bars: 20 μm in A–D; 10 μm in E–G″.

Our study extends previous work that first identified and characterized worms carrying the *n678* mutation (Watanabe *et al.*, 2005, 2007). However, these authors did not describe the drastic changes in cytoskeletal organization and luminal defects that we characterize here. Furthermore, our data are in contrast with the reported rescue of the *sma-5* phenotype by expression in the hypodermis. Instead, we show a complete rescue of the *sma-5* phenotype by intestine-specific reintroduction of a *sma-5* reporter. In accordance, we find a phenocopy of the *sma-5* phenotype, that is, reduced body length, growth retardation, reduced brood size, and shortened life span upon intestine-specific *sma-5(RNAi)*. We therefore conclude that the *sma-5* phenotype is caused by intestine-specific SMA-5 function.

In *sma-5* mutants, a morphologically normal subapical cytoskeleton forms around the lumen of the intestine initially but becomes progressively disorganized over time. We interpret the incremental appearance of the pathological phenotype as a consequence of kinase dysfunction resulting in impaired resilience of the endotube, which manifests as cytoplasmic invaginations upon prolonged and increasing wear and tear. However, the endotube in *sma-5* mutants appears to be fragile and eventually ruptures, perhaps because of stress from normal wear and tear or because of growth during development. The worm intestine seems to be sensitive to stress, and invaginations and luminal dilation occur in worms subjected to challenges such as microbial infection (Estes *et al.*, 2011) or exposure to fungal lectins (Stutz *et al.*, 2015) or pore-forming toxins (Los *et al.*, 2011). In fact, the intestinal filament organizer IFO-1 is up-regulated in response to pore-forming toxins, and this up-regulation requires another MAP kinase, KGB-1 (Kao *et al.*, 2011). In support of a protective role for the SMA-5 MAP kinase, the vertebrate homologue MAPK7 is activated by oxidative stress and hypo-osmolarity (Abe *et al.*, 1996; Chao *et al.*, 1999).

IFO-1 is a critical component of the organization of intermediate filaments in the intestine. During embryogenesis, IFO-1 accumulates at the apical plasma membrane before localization of intermediate filaments (Carberry *et al.*, 2012). Moreover, in *ifo-1* mutants, intermediate filaments collapse onto the CeAJ. In *sma-5* mutants, sites of IFO-1 delamination seem to precede the subsequent herniation of the intermediate filament protein IFB-2 and the lumen of the intestine. We stress, however, that the functions of IFO-1 and SMA-5 are separable, rather than being organized in a simple pathway. Loss of IFO-1 leads to intermediate filament accumulation at junctions, whereas loss of SMA-5 leads to a weakening of the intermediate filament–rich endotube leading to cytoplasmic invaginations. As expected, we find that *sma-5* and *ifo-1* phenotypes are additive in double knockdowns. Furthermore, loss of SMA-5 is coupled to intermediate filament hyperphosphorylation, whereas loss of IFO-1 does not lead to changes in intermediate filament phosphorylation (F.G., unpublished observations). Thus, even though IFO-1 is a potential target of kinases (phosphorylation site database, www.phosida.com), there must be additional SMA-5 targets whose phosphorylation affects intermediate filament phosphorylation and overall apical domain stability. A suppressor screen of the *sma-5* mutants could possibly identify the pathway that links SMA-5 to intermediate filament phosphorylation and network organization. It may also help to understand how and why SMA-5 dysfunction results in two opposing morphologies, namely endotube thinning and endotube thickening. It is possible that phosphorylation of different targets by SMA-5 may be important for network formation and network disassembly.

Our data suggest that the endotube itself becomes organized in a trilaminar structure, with an actin network closest to the plasma membrane anchoring the microvilli, followed by an IFB-2 intermediate filament layer and an IFO-1 layer below. First, we sometimes see that the IFO-1 layer has delaminated and buckled, whereas the IFB-2 layer is still intact. Second, we observe that the actin cytoskeleton is also disrupted in advanced endotube hernias. The observation that the displacement of actin, the actin-binding protein ERM-1,

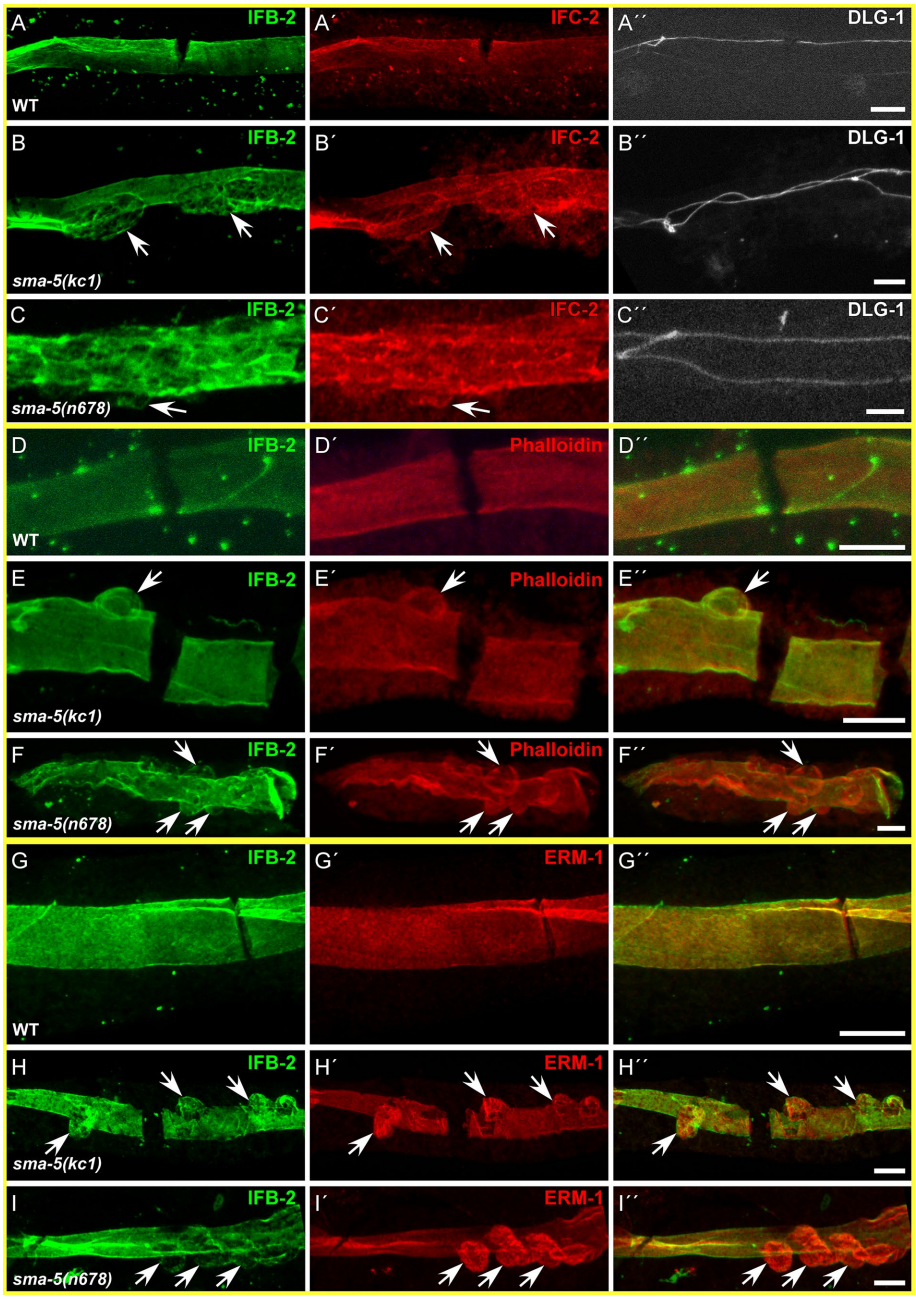


FIGURE 7: The subapical membrane domain invaginates coordinately into the apical cytoplasm of intestinal cells without affecting junction localization in *kc1* and *n678* mutants. The micrographs depict results of fluorescence microscopic detection of apical components in dissected intestines. (A–C″) Triple immunofluorescence detecting the endotube components IFB-2 (left) and IFC-2 (middle) together with the CeAJ component DLG-1 (right) in N2 (WT) and *sma-5* mutants (*sma-5(kc1)*, *sma-5(n678)*). (D–F″) Double fluorescence microscopy localizing IFB-2 with antibodies (left) and F-actin with Alexa Fluor 546–conjugated phalloidin (middle; superimposed images at right) in wild-type and *sma-5* mutant intestines. (G–I″) Double immunofluorescence microscopy using anti-IFB2 (left) and anti-ERM-1 antibodies (middle; merged images at right) in dissected wild-type and mutant intestine. Note the colocalization of IFB-2, IFC-2, F-actin, and ERM-1 in cytoplasmic invaginations (arrows). Scale bars: 10 μm.

IFB-2, and IFC-2 occurs in concert and coincident with the formation of dextran-filled invaginations suggests that the intermediate filament network provides a major scaffolding on which the entire apical membrane domain rests. The existence of cross-bridges among the components in *C. elegans* is also supported by the observation of similar invaginations in *act-5(RNAi)*, *act-5(ok1397)*, *erm-1(RNAi)*, and *ifc-2(RNAi)* intestines (Göbel *et al.*, 2004; Hüsken *et al.*, 2008; Saegusa *et al.*, 2014). In accordance, ultrastructural and molecular links have been described among these components in mice (Hirokawa *et al.*, 1982; Grimm-Günter *et al.*, 2009).

Previous studies in cultured epithelial cells have indicated a role for kinase signaling in epithelial intermediate filament network organization. The ratio of filamentous to soluble keratin correlates with keratin phosphorylation in most, though not all, instances (Chou and Omary, 1993; Liao *et al.*, 1996; Strnad *et al.*, 2002). Furthermore, inhibition of either tyrosine phosphatases or serine–threonine phosphatases resulted in rapid keratin network disruption (Strnad *et al.*, 2001, 2002). Specifically, an involvement of the p38 MAP kinase has been demonstrated in phosphatase inhibitor–induced network disassembly into granular aggregates (Ku *et al.*, 2002; Wöll *et al.*, 2007). In accordance, stimulation of p38 activity induced network disorganization, leading to the formation of large granules containing phosphorylated keratins (Wöll *et al.*, 2007). JNK and p38 MAP kinase–dependent keratin phosphorylation has been described for several stress paradigms such as osmotic imbalance and heat and chemical stress (D'Alessandro *et al.*, 2002; Ku *et al.*, 2002; Wöll *et al.*, 2007). It was further shown that cooperation between p38 MAP kinase and MAPKAP kinase MK2/3 is responsible for keratin phosphorylation in intestinal HT29-MTX cells (Menon *et al.*, 2010). Remarkably, MK2-deficient mice become less sensitive to dextran sodium sulfate (DSS)-induced colitis (Li *et al.*, 2013). This situation is analogous to that encountered in our *sma-5* mutants. We suggest that the protective effect against stress is mediated in both instances by reduced intermediate filament phosphorylation resulting in a more resilient filament network. Furthermore, similar mechanisms may act in other cell systems. Thus it has been demonstrated that tension induces a mechanotransduction pathway in the *C. elegans* hypodermis, whose output is increased intermediate filament phosphorylation (Zhang *et al.*, 2011). It also involves a kinase (PAK-1) whose activity is stimulated by a hemidesmosomal mechanosensor acting through hemidesmosomal adaptor proteins and the Rac GTPase CED-10. It will be interesting to find out whether similar pathways involving SMA-5 exist in the *C. elegans* intestine.

The evolutionary conservation of the subapical distribution of intermediate filaments anchored to the apical junctional complex, either in the form of the prominent endotube in *C. elegans* or as a dense network below the terminal web in *Isotumurus maculatus* (Mencarelli *et al.*, 2011), to mouse (Hirokawa *et al.*, 1982) and man

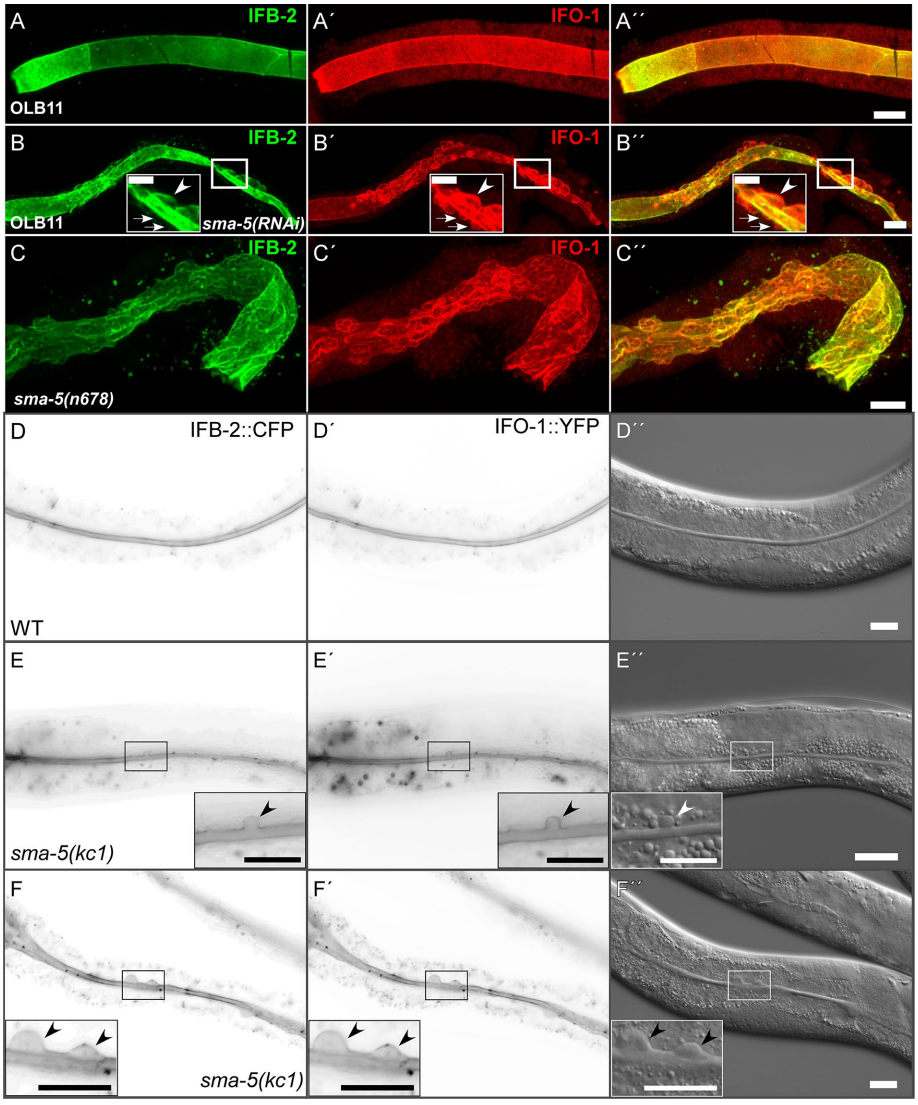


FIGURE 8: Intestine-specific *sma-5(RNAi)* animals and *sma-5* mutants develop IFB-2- and IFO-1–positive cytoplasmic invaginations. (A–C″) Antibody staining detecting IFB-2 and IFO-1 in the dissected adult intestine of intestine-specific RNAi strain OLB11 (A–A″), OLB11 treated with *sma-5(RNAi)* (B–B″), and *sma-5(n678)* mutants (C–C″). (D–F″) In vivo fluorescence detection of IFB-2::CFP and IFO-1::YFP (inverted presentation in D, D′; E, E′, F, F′; corresponding interference contrast images in D″, E″, F″, respectively) in wild-type strain BJ276 (WT; D–D″) and *sma-5(kc1)* animals of strain BJ277 (E–F″). The images depict the characteristic apical colocalization of IFB-2 and IFO-1 that is maintained in the cytoplasmic invaginations forming in the mutant backgrounds. Note that invaginations are usually marked by both (arrowheads), although occasionally IFO-1–positive invaginations lack IFB-2 (e.g., arrows in B–B″). Scale bars: 10 µm in A–C″; 20 µm in D–F″; 10 µm in insets of E–E′; 20 µm in insets of F–F′; 5 µm in insets of B–B″.

(Mooseker, 1985; Carboni *et al.*, 1987) can be taken as evidence for the functional importance of this arrangement. The small body size, reduced brood size, developmental retardation, and reduced life span observed in *sma-5* mutants (this study) and *ifo-1* mutants (unpublished data; Carberry *et al.*, 2012) all strongly support this notion. In addition, mechanical functions have been ascribed to intestinal intermediate filaments (Jahnel *et al.*, 2016) and keratin mutations have been linked to intestinal inflammation in mice lacking keratins (Baribault *et al.*, 1994; Habtezion *et al.*, 2005). Interestingly, keratin polymorphisms have been associated with intestinal bowel disease in human patients (Owens and Lane, 2004; Owens *et al.*, 2004; Zupancic *et al.*, 2014). In vitro observations provide further support for a function of intermediate filaments in intestinal barrier formation and its regulation by phosphorylation. Thus interleukin-6 (IL-6) activity evoked increasing phosphorylation of keratins 8 and 18 coincident with subapical intermediate filament accumulation in cultured colon carcinoma–derived Caco2-BBE cells (Wang *et al.*, 2007). In accordance, IL-6 knockout mice presented with reduced keratin 8 levels and showed increased intestinal permeability after administration of dextran sulfate sodium (DSS) (Wang *et al.*, 2007). The relationship between intestinal barrier function and keratin phosphorylation is also suggested by the work of Tao *et al.* (2006), who demonstrated that hypo-osmosis induced site-specific dephosphorylation of keratin 8 in HT29 cells, whereas hyper-osmosis induced keratin 8 hyperphosphorylation. These observations are in contrast to reports in the same study noting keratin hyperphosphorylation in human HRT18 and Caco2 cells and in ex vivo colon cultures upon hypo-osmosis. But they also underscore the importance, though presently poorly understood relevance, of intermediate filament phosphorylation in different stress paradigms.

Taking these findings together, we conclude that intermediate filaments are crucial ingredients for the maintenance of the *C. elegans* intestinal tube, which is an important prerequisite for efficient food uptake. It is likely that they fulfill similar functions in other lumen-containing epithelial structures such as the excretory cells in *C. elegans* (Kolotuev *et al.*, 2013).

## MATERIALS AND METHODS

### DNA constructs

Fosmid WRM0633B_G09(pRedFlp-Hgr)(sma-5[26688]::S0001_pR6K_Amp_2xTY1ce_EGFP_FRT_rpsl_neo_FRT_3xFlag)dFRT::unc-119-Nat (here referred to as fosmid 3170) was obtained from the TransgeneOme Project of the Max Planck Institute of Molecular Cell Biology and Genetics (Sarov *et al.*, 2006; TransgeneOme Project, https://transgeneome.mpi-cbg.de/transgeneomics/index.html). pWD553 was made by first cloning the *sma-5* cDNA into the *Pst*I-*Xma*I sites of plasmid *pPifb-2:cfp* (1759; Hüsken *et al.*, 2008). Next the *ifb-2* promoter was replaced by the *vha-6* promoter. This was done with a Gibson reaction (Gibson *et al.*, 2009) of two fragments. The first fragment was a *Pst*I-*Hin*dIII digest. The second was a PCR of the *vha-6* promoter using primers TAACAACTTGGAAATGAAATAAGCTTaagtatactatttattactcgatacttttgttca and TGTGGAGGAGACATCTGCAGttttttatgggttttggtaggttttagtcgccctg. The PCR template was pML25 [*vha-6p*]. pWD554 was made by replacing the *cfp* coding sequence and the *unc-54* 3′-untranslated region (UTR) of pWD553 with the *let-858* 3′ UTR. This was done with a Gibson reaction (Gibson *et al.*, 2009) of

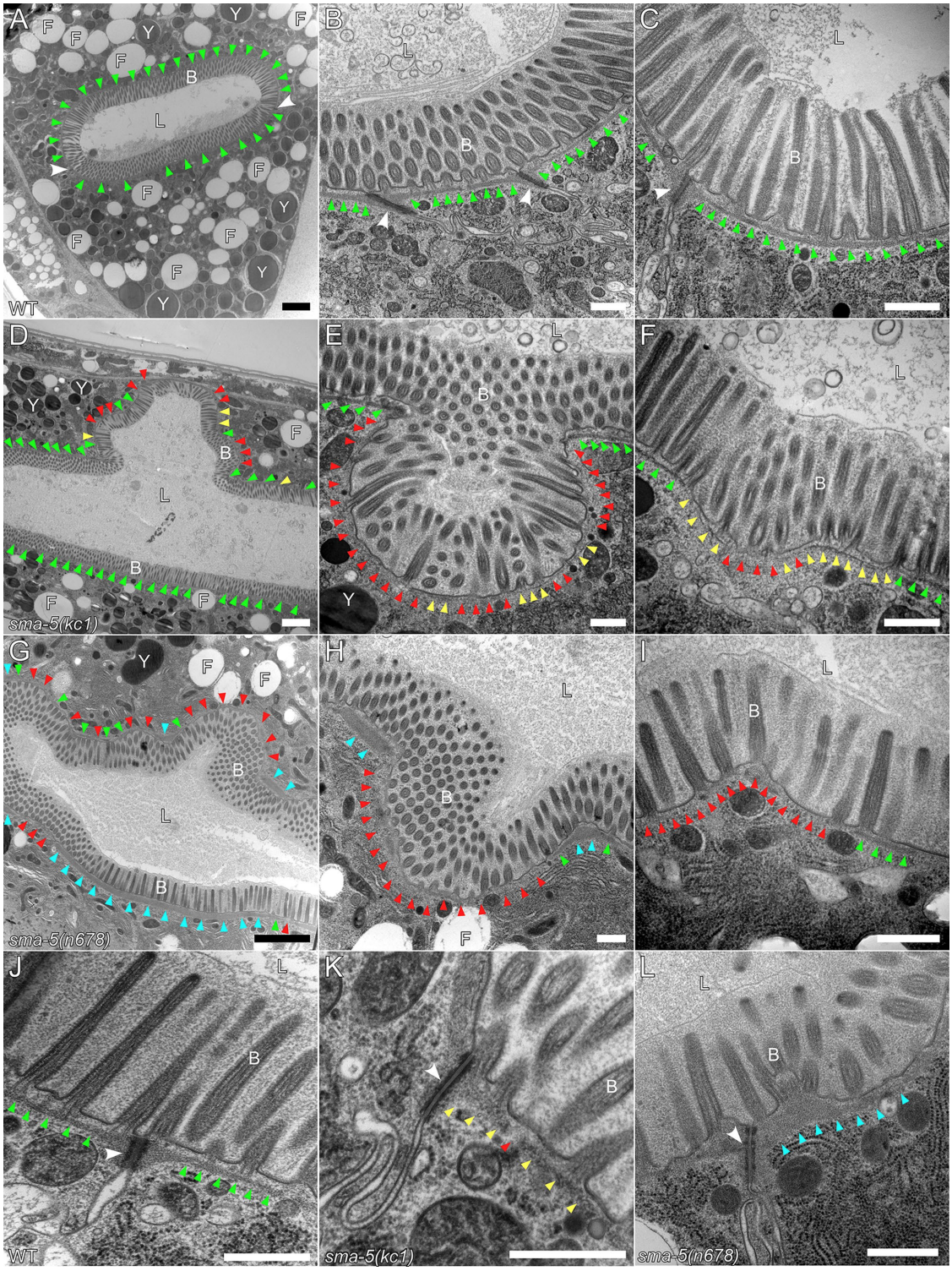


FIGURE 9: Luminal perturbations, disordered microvilli, and endotube alterations with local gaps are present in the intestine of *sma-5* mutants. The electron micrographs are taken from wild type (transverse sections, A–C, J), *sma-5(kc1)* (longitudinal sections, D–F, K), and *sma-5(n678)* mutants (longitudinal sections, G–I, L). Differently sized luminal invaginations into the cytoplasm of enterocytes are seen in both mutants (D–H). Note that the endotube layer is indistinguishable from that of the wild type in some regions (green arrowheads) but is drastically altered in other regions. In *sma-5(kc1)* local endotube thinning (yellow arrowheads) and endotube gaps (red arrowheads) are observed. In *sma-5(n678)*, localized and extensive endotube thickening (blue arrowheads) and thinning (yellow arrowheads) with complete endotube loss (red arrowheads) are frequent. Note also that loss of endotube and endotube thinning coincide with the rim of cytoplasmic invaginations (E, F, and H). In addition, the brush border (B) is irregular in many regions, with variable spacing and orientation (e.g., I and L). The CeAJ appears unperturbed (white arrowheads in A–C, J–L) and is still associated with the material of the endotube. L, lumen; Y, yolk granule; F, lipid droplet. Scale bars: 2 µm in A, D, and G; 500 nm in B–C, E–F, and H–L.

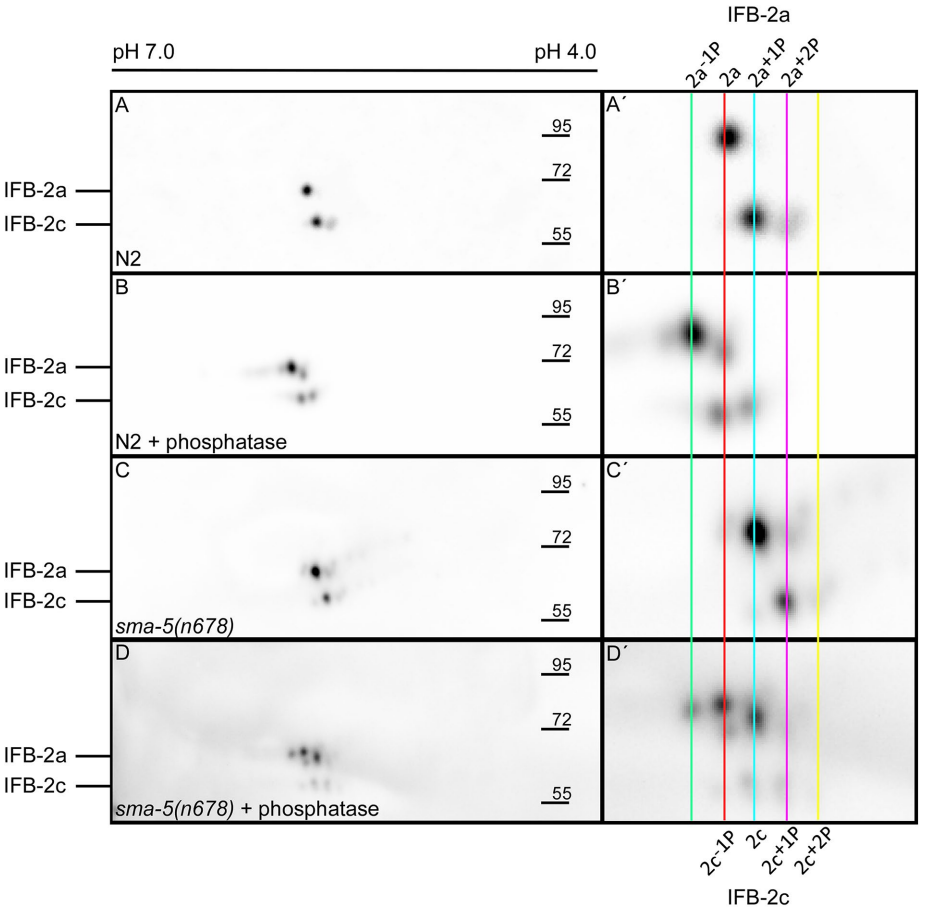


FIGURE 10: Two-dimensional immunoblot analysis of IFB-2 detects SMA-5–dependent phosphorylation. The picture shows immunoblots of polypeptides obtained from total worm lysates that were separated by two-dimensional isoelectric focusing gel electrophoresis (pH gradient of second dimension indicated on top) and reacted with monoclonal anti–IFB-2 antibodies. The higher magnifications at right depict details of the different IFB-2 isoforms that were detected. They differ in size (larger a and smaller c variant) and isoelectric points as a consequence of phosphorylation (+P, –P). Note that, at steady state, one a variant (denoted 2a) and two c variants, that is, a major spot denoted as 2c and a minor spot denoted as $2c^{+1P}$, are visible in the wild-type N2 background. As expected, phosphatase treatment leads to a shift to more basic isoelectric points ($2a^{-1P}$ and $2c^{-1P}$). In contrast, isoelectric points are shifted toward acidic in the *sma-5(n678)* background, with new spots at $2a^{+1P}$, $2a^{+2P}$, and $2c^{+2P}$. Again, phosphatase treatment shifts the variants toward the nonphosphorylated positions. Indication of molecular weight in kilodaltons.

two fragments. The first was a *Sma*I-*Spe*I digest of pWD553. The second was a PCR of the *let-858* UTR using the primers ATTGCGCAGCAACCCGGGTAAcTCGACGCCaACGTCGTTGAattttc and GGCCCGTACGGCCGAAACCAAGCGAGGACAATTCTcatcg and pADA126 (Watanabe *et al.*, 2011) as a template. pWD555 was made by adding three native introns into the *sma-5* cDNA. This was done using a Gibson reaction (Gibson *et al.*, 2009) of two fragments. The first was a *Bam*HI-*Bgl*II digest of pWD554, and the second was a PCR from worm genomic DNA using primers tcttcatcatatcatttatggaaacgaggatccattggaggaaca and catgctgatcaattcttgatgattgagatcttcaacttgcatc. The *sma-5(RNAi)* feeding vector was produced by cloning the coding sequence of W06B3.2a exon 5 into the *Xba*I/*Bam*HI restriction sites of vector L4440 (Addgene, Cambridge, MA) using forward primer ACGGATCCTATCTTCATGCTGCATGCATCGCT and reverse primer ACTCTAGAATCATCTCCTCGAGCTTTGCAGAA.

### *C. elegans* strains

Wild-type Bristol strain N2 and Hawaiian strain CB4856 were obtained from the *Caenorhabditis* Genetics Center (CGC; University of Minnesota, Minneapolis, MN). Strain BJ52 *kcIs21[ifb-2p::ifb2::cfp]V* was recently described (Hüsken *et al.*, 2008; for chromosomal mapping, see Hüsken, 2008). *sma-5* mutant strains carrying allele *kc1* were BJ132 *sma-5(kc1)X;kcIs21[ifb-2p::ifb-2::cfp]V* and BJ141 *sma-5(kc1)X*. Strain FK312 *sma-5(n678)X* (Watanabe *et al.*, 2007) was provided by the CGC. It was crossed with BJ49 *kcIs6[ifb-2p::ifb-2::cfp]IV* (Hüsken *et al.*, 2008; for chromosomal mapping, see Hüsken, 2008) to obtain strain OLB18 *sma-5(n678)X;kcIs6[ifb2-p::ifb-2::cfp]IV*. BJ276 *kcIs30[ifo-1p::ifo-1::yfp;myo-3p::mCherry::unc-54];kcIs21[ifb-2p::ifb2::cfp]V* and BJ277 *sma-5(kc1)X;kcIs30[ifo-1p::ifo-1::yfp,myo-3p::mCherry::unc-54];kcIs21[ifb-2p::ifb2::cfp]V* were both generated in one step by crossing BJ132 with BJ186 *kcIs30[ifo-1p::ifo-1::yfp;myo-3p::mCherry::unc-54]III* animals. Microinjection of fosmid 3170 into the gonad of DP38 *unc-119(ed3)* animals (provided by the CGC) resulted in strain BJ263 *kcEx73[pRedFlp-Hgr)(sma-5[26688]::S0001_pR6K_Amp_2xTY1ce_EGFP_FRT_rpsl_neo_FRT_3xFlag)dFRT::unc-119-Nat]* producing SMA-5::EGFP. Rescue strain BJ269 *sma-5(kc1)X;kcEx73[pRedFlp-Hgr)(sma-5[26688]::S0001_pR6K_Amp_2xTY1ce_EGFP_FRT_rpsl_neo_FRT_3xFlag)dFRT::unc-119-Nat]* was generated by microinjection of fosmid 3170 into BJ141 *sma-5(kc1)X* animals. Rescue strains BJ300/301 *sma-5(n678)X; kcEx75[vha-6p::sma-5;myo-2p::gfp::H2B]* were generated by microinjection of plasmid pWD555 and pCFJ770 [*myo-2p::gfp::H2B]* into OLB18 animals. Microinjection of plasmid 1772 [*ifb-2p::ifb-2::cfp*] (Hüsken *et al.*, 2008) into the gonad of strain EC668 *kcEx41[unc-119(+);ifa-1a::gfp];unc-119(ed3)III* (Karabinos *et al.*, 2003) yielded strain BJ37 *kcEx4[ifb-2p::ifb-2::cfp]; kcEx41[unc-119(+);ifa-1a::gfp];unc-119(ed3)III*. Strain OLB11 *rde-1(ne219)*; *kcIs39*[pOLB11 (*elt-2p::rde-1(+)*); pRF4(*rol-6(su1006)*)], which allows intestine-specific RNAi, was previously described (Pilipiuk *et al.*, 2009). Maintenance and propagation of strains was done as previously described (Brenner, 1974).

### RNAi

RNAi by feeding was performed as previously described (Hüsken *et al.*, 2008) with minor modifications. Nematode growth medium (NGM) plates contained 100 µg/ml ampicillin, 12.5 µg/ml tetracycline, and 2 mM isopropyl β-D-1-thiogalactopyranoside (IPTG). Plasmid clones for RNAi were either taken from the Ahringer RNAi library (Geneservice, Cambridge, UK) or obtained by

cloning gene sequences of at least 500 base pairs containing a minimum of one coding exon into the feeding vector L4440 (Addgene) followed by chemical transformation into RNaseIII-deficient HT115 *Escherichia coli*. Liquid overnight cultures in Luria broth with 100 µg/ml ampicillin and 12.5 µg/ml tetracycline were supplemented with 7 µl/ml 1 M IPTG before plates were inoculated with a volume of 300 µl each. After overnight incubation at room temperature, 10–20 L4 larvae were added; this was followed by incubation at 15°C or 18°C. After 48 h, adult grown animals were transferred to new plates and incubated as before until $F_1$ progeny could be analyzed. Alternatively, RNAi by microinjection was performed. To this end, dsRNA was first amplified in vitro using the MAXIscript T7 Kit (Ambion, Austin, TX) and then injected into L4 larvae using the inverse Leica DM IRB microscope (Leica, Wetzlar, Germany). Injected animals were subsequently incubated for 24 h at 20°C on normal NGM plates and transferred onto new plates for examination of $F_1$ progeny.

### Isolation and identification of *sma-5* mutants

BJ52 *kcIs21[ifb-2p::ifb2::cfp]V* animals were subjected to chemical mutagenesis by incubating adult worms with 47 mM ethyl methane sulfonate for 4 h at room temperature. $F_2$ progeny corresponding to 10,000 haploid genomes were screened for alterations of IFB-2::CFP fluorescence. Isolated animals were backcrossed five times with N2 to obtain strain BJ132 *sma-5(kc1)X;kcIs21[ifb-2p::ifb-2::cfp] V*. Further identification of the mutated gene was done by single-nucleotide polymorphism mapping (Davis *et al.*, 2005; Carberry *et al.*, 2012) and RNAi targeting of the remaining 94 candidate genes within the mapped region. An RNAi screen was performed by bacterial feeding (Ahringer library) starting either with L1 or L4 larva of strain BJ52 at 18°C or 20°C, resulting in down-regulation of post-embryonic or embryonic gene function, respectively. In some instances, RNAi by microinjection of dsRNA was also performed, when appropriate feeding clones were not available. Animals were screened for a copy of the *sma-5(kc1)* phenotype using a fluorescence binocular.

### Immunostaining and fluorescence labeling

For immunohistology, animals were dissected in phosphate-buffered saline on a poly-L-lysine–coated glass slide; this was followed by mounting a coverslip on top, removing excessive fluid, and freezing the sample in liquid nitrogen. The coverslip was then blasted off, resulting in permeabilization of the cuticle. Samples were then fixed by incubation at –20°C first for 10 min in methanol and then for 20 min in acetone, followed by incubation in a graded ethanol series (5 min in 90% ethanol at –20°C, 5 min in 60% ethanol at –20°C, and 5 min in 30% ethanol at room temperature). After a 10 min washing in TBST (TBS buffer [20 mM (wt/vol) Tris(hydroxymethyl)-aminomethane, pH 7.6, 0.15 M (wt/vol) NaCl] + 0.2% Tween 20), samples were incubated with primary antibodies dissolved in blocking solution (1% [wt/vol] nonfat milk powder [Roth, Karlsruhe, Germany], 1% [wt/vol] bovine serum albumin, and 0.02% [wt/vol] sodium azide) overnight at 4°C. Following a 10 min wash in TBST, samples were incubated with secondary antibodies dissolved in blocking solution for 2 h at room temperature. After a final wash for 10 min in TBST, samples were embedded in Mowiol 4–88 (Sigma, St. Louis, MO) supplemented with DABCO (Roth) and covered with a glass coverslip. The following primary antibodies were used: guinea pig anti–IFO-1 (1:100; Carberry *et al.*, 2012), guinea pig anti–IFC-2 (1:10; Karabinos *et al.*, 2002), rabbit anti-DLG-1 (1:200; Segbert *et al.*, 2004), rabbit anti–ERM-1 (1:200; van Fürden *et al.*, 2004), mouse monoclonal anti–IFB-2 (MH33, 1:200; Francis and Waterston, 1985), rabbit anti–GFP (1:1000; Invitrogen, Carlsbad, CA), and mouse monoclonal anti–AJM-1 (MH27, 1:200; Francis and Waterston, 1985). Secondary antibodies used at 1:200 dilution were Cy2-, Cy3-conjugated affinity-purified anti-mouse immunoglobulin G (IgG; Rockland, Limerick, PA), Alexa Fluor 488–conjugated affinity-purified anti-mouse IgG (Invitrogen), Alexa Fluor 555–conjugated affinity-purified anti-mouse IgG (Invitrogen), Dylight488- and Cy3-conjugated affinity-purified anti–guinea pig IgG, Cy2-, Cy3-, Cy5-conjugated anti-rabbit IgG (Jackson ImmunoResearch Laboratories, West Grove, PA), and Alexa Fluor 488–conjugated affinity-purified anti-rabbit IgG (Invitrogen). Actin filaments were stained by Alexa Fluor 546–phalloidin (Molecular Probes, Eugene, OR).

To label the intestinal lumen and to check for intestinal tightness, young adults were incubated on agar plates containing 100 µl of 0.3% (wt/vol) Texas Red–conjugated dextran (10,000 MW; Molecular Probes) in the presence of OP50 bacteria at room temperature for 24 h. They were subsequently washed three times in M9 medium before being imaged.

### Microscopy

Microscopy was performed with confocal laser-scanning microscopes (LSM 510 META and LSM 710, Zeiss; Jena, Germany; TCS SP5; Leica), a Zeiss Apotome fitted with a Zeiss AxioCamMRm camera, and a Zeiss Axioplan 2 fitted with an ORCA-ER camera (Hamamatsu, Herrsching, Germany). For electron microscopy, worms were cryofixed by rapid high-pressure freezing with the help of a Leica EM Pact high-pressure freezer. For each genotype, at least 10 samples, each consisting of 5–15 worms, were fixed. Quick-freeze substitution was done using two alternative fixatives: 1) 1% $OsO_4$, 0.2% uranyl acetate in acetone; and 2) 1% $OsO_4$, 0.5% uranyl acetate, and 5% $H_2O$ in acetone. Embedding into epoxy resin was performed as previously described (McDonald and Webb, 2011). Following quick-freeze substitution, 50 nm transverse and longitudinal ultrathin sections of the worms were prepared with a Leica UC6/FC6 ultramicrotome, contrasted for 10 min each in 1% uranyl acetate in ethanol followed by Reynolds lead citrate. Sections were viewed at 100 kV with a Hitachi H-7600 transmission electron microscope (Tokyo, Japan).

### Immunoblotting

For each assay, 60 adult worms of the wild type or 120 *sma-5(n678)* mutant animals were handpicked, transferred into 30 µl $dH_2O$, and immediately frozen at –80°C. After quick thawing, samples were sucked up and down through a 30G hypodermic syringe (BD Medical, Heidelberg, Germany) three times. Subsequently, 7.5 µl of 5× Laemmli loading buffer was added, and samples were incubated for 5 min at 90°C. Proteins were separated in a 10% SDS polyacrylamide gel, and transferred onto polyvinylidene difluoride membrane by wet-tank blotting at 100 V for 60 min. The membranes were blocked for 1–2 h at room temperature in Roti-Block (Roth) and then incubated with primary antibodies in Roti-Block at 4°C overnight. Antibodies against total ERM-1 (murine monoclonal antibodies from the Developmental Studies Hybridoma Bank [DHSB, Iowa City, IA]; Hadwiger *et al.*, 2010) were diluted 1:1000, against phosphorylated ERM-1 (rabbit monoclonal antibodies ab76247 from Abcam, Cambridge, UK) 1:500, and against actin (rabbit polyclonal antibodies A2066 from Sigma) 1:1000. Three 10 min washings with TBST (20 mM Tris(hydroxymethyl)-aminomethane, 0.15 M NaCl, 0.1% Tween 20 [vol/vol], pH 7.6) ensued. Incubation with secondary antibodies (goat anti-mouse IgG antibodies and goat anti-rabbit IgG antibodies coupled to horseradish peroxidase from DAKO

[Santa Clara, CA] at 1:5000 in Roti-Block) was done for 1 h at room temperature. Final washes (three at 10 min each) were in TBST. Bound antibodies were detected with Fusion Solo (Vilber, Eberhardzell, Germany) using chemiluminescence substrate AceGlow (Peqlab, Darmstadt, Germany).

For two-dimensional gel electrophoresis, 60 adult worms were handpicked for each assay, transferred into 15 µl $dH_2O$, and immediately frozen at −80°C. After quick thawing, each sample was aspirated by a syringe needle three times, resulting in homogenization, and stored on ice for at least 30 min after addition of 15 µl 2× lysis buffer (9.5 M urea, 4% [wt/wt] 3-[(3-cholamidopropyl)dimethylammonio]-1-propanesulfonate, 0.04% [wt/vol] bromophenol blue, 2% [wt/vol] dithiothreitol [DTT], 2% [vol/vol] Immobilized pH Gradients buffer [GE Healthcare, Freiburg, Germany]). Then 170 µl 2× lysis buffer was added, and all of the solution (200 µl) was transferred to an Immobiline DryStrip (pH 4-7, 11 cm; GE Healthcare) for overnight rehydration. During this time, the strip was covered by silicone oil to prevent sulfuring of urea. For isoelectric focusing, the following protocol was used: 150 V, 75 V/h; 300 V, 225 V/h; 1000 V, 500 V/h; and 3000 V, 27,000 V/h. Strips were sometimes stored at −80°C until further usage. For subsequent immunoblot analysis, strips were first washed for 15 min in 0.1 g DTT/10 ml equilibration buffer (6 M urea, 2% [wt/vol] SDS, 50 mM [wt/vol] Tris(hydroxymethyl)-aminomethane, pH 8.8, 0.02% [wt/vol] bromophenol blue, 30% [vol/vol] glycerol); this was followed by another washing step for 15 min in 0.25 g iodoacetamide/10 ml equilibration buffer. Strips were then placed on top of the solidified stacking gel and further embedded by agarose (0.5% [wt/vol] agarose, 0.02% [wt/vol] bromophenol blue in running buffer [0.25 M Tris(hydroxymethyl)-aminomethane, 1.92 M [wt/vol] glycine, 1% [wt/vol] SDS]). After gel electrophoretic separation, proteins were transferred onto polyvinylidene difluoride membrane by tank blotting at 100 V for 70 min. After blocking for 1–2 h at room temperature in Roti-Block (Roth), immunostaining against IFB-2 was done by incubating the blots with primary antibody MH33 (1:1000 dilution in Roti-Block) at 4°C overnight, washing 3 × 10 min in TBST, incubating with secondary mouse anti-mouse IgG antibodies coupled to horseradish peroxidase from DAKO at 1:5000 in Roti-Block, diluting for 1 h at room temperature, and administering final washes in TBST. Bound antibodies were detected with Fusion Solo using chemiluminescence substrate AceGlow.

## ACKNOWLEDGMENTS

We thank Bärbel Bonn and Sabine Eisner for superb technical support and students Carina Keller and Carina Eherer for their help. This work was supported by grants from the German Research Council (LE566/14-1, LE566/14-3, BO 1061/11-1, and BO1061/11-3). Some strains were provided by the CGC, which is funded by National Institutes of Health (NIH) Office of Research Infrastructure Programs (P40 OD010440). The monoclonal antibodies MH27 and MH33 developed by Waterston and ERM-1 (Hadwiger *et al.*, 2010) were obtained from the Developmental Studies Hybridoma Bank, created by the National Institute of Child Health and Human Development of the NIH and maintained at the Department of Biology, University of Iowa. We also acknowledge Anton Karabinos for generously sharing anti–IFC-2 antibody. Fosmids were obtained from the TransgeneOme Project of the MPI-CBG. Plasmid pML25 was generously shared by Matt Labella. Plasmid pCFJ770 was obtained from Christian Frøkjær-Jensen.

## REFERENCES

Abe J, Kusuhara M, Ulevitch RJ, Berk BC, Lee JD (1996). Big mitogen-activated protein kinase 1 (BMK1) is a redox-sensitive kinase. J Biol Chem 271, 16586–16590.

Baribault H, Penner J, Iozzo RV, Wilson-Heiner M (1994). Colorectal hyperplasia and inflammation in keratin 8-deficient FVB/N mice. Genes Dev 8, 2964–2973.

Bossinger O, Fukushige T, Claeys M, Borgonie G, McGhee JD (2004). The apical disposition of the *Caenorhabditis elegans* intestinal terminal web is maintained by LET-413. Dev Biol 268, 448–456.

Brenner S (1974). The genetics of *Caenorhabditis elegans*. Genetics 77, 71–94.

Carberry K, Wiesenfahrt T, Geisler F, Stocker S, Gerhardus H, Uberbach D, Davis W, Jorgensen E, Leube RE, Bossinger O (2012). The novel intestinal filament organizer IFO-1 contributes to epithelial integrity in concert with ERM-1 and DLG-1. Development 139, 1851–1862.

Carberry K, Wiesenfahrt T, Windoffer R, Bossinger O, Leube RE (2009). Intermediate filaments in *Caenorhabditis elegans*. Cell Motil Cytoskeleton 66, 852–864.

Carboni JM, Howe CL, West AB, Barwick KW, Mooseker MS, Morrow JS (1987). Characterization of intestinal brush border cytoskeletal proteins of normal and neoplastic human epithelial cells. A comparison with the avian brush border. Am J Pathol 129, 589–600.

Chambers C, Grey RD (1979). Development of the structural components of the brush border in absorptive cells of the chick intestine. Cell Tissue Res 204, 387–405.

Chao TH, Hayashi M, Tapping RI, Kato Y, Lee JD (1999). MEKK3 directly regulates MEK5 activity as part of the big mitogen-activated protein kinase 1 (BMK1) signaling pathway. J Biol Chem 274, 36035–36038.

Chou CF, Omary MB (1993). Mitotic arrest-associated enhancement of *O*-linked glycosylation and phosphorylation of human keratins 8 and 18. J Biol Chem 268, 4465–4472.

Coch RA, Leube RE (2016). Intermediate filaments and polarization in the intestinal epithelium. Cells 5, 32.

D'Alessandro M, Russell D, Morley SM, Davies AM, Lane EB (2002). Keratin mutations of epidermolysis bullosa simplex alter the kinetics of stress response to osmotic shock. J Cell Sci 115, 4341–4351.

Davis MW, Hammarlund M, Harrach T, Hullett P, Olsen S, Jorgensen EM (2005). Rapid single nucleotide polymorphism mapping in *C. elegans*. BMC Genomics 6, 118.

Estes KA, Szumowski SC, Troemel ER (2011). Non-lytic, actin-based exit of intracellular parasites from *C. elegans* intestinal cells. PLoS Pathog 7, e1002227.

Fath KR, Burgess DR (1995). Microvillus assembly. Not actin alone. Curr Biol 5, 591–593.

Fehon RG, McClatchey AI, Bretscher A (2010). Organizing the cell cortex: the role of ERM proteins. Nat Rev Mol Cell Biol 11, 276–287.

Fievet B, Louvard D, Arpin M (2007). ERM proteins in epithelial cell organization and functions. Biochim Biophys Acta 1773, 653–660.

Francis GR, Waterston RH (1985). Muscle organization in *Caenorhabditis elegans*: localization of proteins implicated in thin filament attachment and I-band organization. J Cell Biol 101, 1532–1549.

Geisler F, Leube RE (2016). Epithelial intermediate filaments: guardians against microbial infection? Cells 5, 29.

Gibson DG, Young L, Chuang RY, Venter JC, Hutchison CA, Smith HO (2009). Enzymatic assembly of DNA molecules up to several hundred kilobases. Nat Methods 6, 343–345.

Göbel V, Barrett PL, Hall DH, Fleming JT (2004). Lumen morphogenesis in *C. elegans* requires the membrane-cytoskeleton linker erm-1. Dev Cell 6, 865–873.

Grimm-Günter EM, Revenu C, Ramos S, Hurbain I, Smyth N, Ferrary E, Louvard D, Robine S, Rivero F (2009). Plastin 1 binds to keratin and is required for terminal web assembly in the intestinal epithelium. Mol Biol Cell 20, 2549–2562.

Habtezion A, Toivola DM, Butcher EC, Omary MB (2005). Keratin-8-deficient mice develop chronic spontaneous Th2 colitis amenable to antibiotic treatment. J Cell Sci 118, 1971–1980.

Hadwiger G, Dour S, Arur S, Fox P, Nonet ML (2010). A monoclonal antibody toolkit for *C. elegans*. PLoS One 5, e10161.

Hirokawa N, Tilney LG, Fujiwara K, Heuser JE (1982). Organization of actin, myosin, and intermediate filaments in the brush border of intestinal epithelial cells. J Cell Biol 94, 425–443.

Homberg M, Ramms L, Schwarz N, Dreissen G, Leube RE, Merkel R, Hoffmann B, Magin TM (2015). Distinct impact of two keratin mutations causing epidermolysis bullosa simplex on keratinocyte adhesion and stiffness. J Invest Dermatol 135, 2437–2445.

Hüsken K (2008). Identifizierung und Charakterisierung von Intermediärfilament-Organisatoren in *Caenorhabditis elegans*. PhD Thesis. Mainz, Germany: Johannes Gutenberg-Universität Mainz.

Hüsken K, Wiesenfahrt T, Abraham C, Windoffer R, Bossinger O, Leube RE (2008). Maintenance of the intestinal tube in *Caenorhabditis elegans*: the role of the intermediate filament protein IFC-2. Differentiation 76, 881–896.

Iwatsuki H, Suda M (2010). Seven kinds of intermediate filament networks in the cytoplasm of polarized cells: structure and function. Acta Histochem Cytochem 43, 19–31.

Jahnel O, Hoffmann B, Merkel R, Bossinger O, Leube RE (2016). Mechanical probing of the intermediate filament-rich *Caenorhabditis elegans* intestine. Methods Enzymol 568, 681–706.

Kao CY, Los FC, Huffman DL, Wachi S, Kloft N, Husmann M, Karabrahimi V, Schwartz JL, Bellier A, Ha C, *et al.* (2011). Global functional analyses of cellular responses to pore-forming toxins. PLoS Pathog 7, e1001314.

Karabinos A, Schulze E, Klisch T, Wang J, Weber K (2002). Expression profiles of the essential intermediate filament (IF) protein A2 and the IF protein C2 in the nematode *Caenorhabditis elegans*. Mech Dev 117, 311–314.

Karabinos A, Schulze E, Schunemann J, Parry DA, Weber K (2003). In vivo and in vitro evidence that the four essential intermediate filament (IF) proteins A1, A2, A3 and B1 of the nematode *Caenorhabditis elegans* form an obligate heteropolymeric IF system. J Mol Biol 333, 307–319.

Kim S, Coulombe PA (2007). Intermediate filament scaffolds fulfill mechanical, organizational, and signaling functions in the cytoplasm. Genes Dev 21, 1581–1597.

Kolotuev I, Hyenne V, Schwab Y, Rodriguez D, Labouesse M (2013). A pathway for unicellular tube extension depending on the lymphatic vessel determinant Prox1 and on osmoregulation. Nat Cell Biol 15, 157–168.

Ku NO, Azhar S, Omary MB (2002). Keratin 8 phosphorylation by p38 kinase regulates cellular keratin filament reorganization: modulation by a keratin 1-like disease causing mutation. J Biol Chem 277, 10775–10782.

Ku NO, Zhou X, Toivola DM, Omary MB (1999). The cytoskeleton of digestive epithelia in health and disease. Am J Physiol 277, G1108–G1137.

Li YY, Yuece B, Cao HM, Lin HX, Lv S, Chen JC, Ochs S, Sibaev A, Deindl E, Schaefer C, Storr M (2013). Inhibition of p38/Mk2 signaling pathway improves the anti-inflammatory effect of WIN55 on mouse experimental colitis. Lab Invest 93, 322–333.

Liao J, Ku NO, Omary MB (1996). Two-dimensional gel analysis of glandular keratin intermediate filament phosphorylation. Electrophoresis 17, 1671–1676.

Los FC, Kao CY, Smitham J, McDonald KL, Ha C, Peixoto CA, Aroian RV (2011). RAB-5- and RAB-11-dependent vesicle-trafficking pathways are required for plasma membrane repair after attack by bacterial pore-forming toxin. Cell Host Microbe 9, 147–157.

Magin TM, Vijayaraj P, Leube RE (2007). Structural and regulatory functions of keratins. Exp Cell Res 313, 2021–2032.

Markl J, Franke WW (1988). Localization of cytokeratins in tissues of the rainbow trout: fundamental differences in expression pattern between fish and higher vertebrates. Differentiation 39, 97–122.

Maurizii MG, Alibardi L, Taddei C (2000). Organization and characterization of the keratin cytoskeleton in the previtellogenic ovarian follicle of the lizard *Podarcis sicula* Raf. Mol Reprod Dev 57, 159–166.

McDonald KL, Webb RI (2011). Freeze substitution in 3 hours or less. J Microsc 243, 227–233.

Mencarelli C, Ciolfi S, Caroti D, Lupetti P, Dallai R (2011). Isomin: a novel cytoplasmic intermediate filament protein from an arthropod species. BMC Biol 9, 17.

Mendez MG, Restle D, Janmey PA (2014). Vimentin enhances cell elastic behavior and protects against compressive stress. Biophys J 107, 314–323.

Menon MB, Schwermann J, Singh AK, Franz-Wachtel M, Pabst O, Seidler U, Omary MB, Kotlyarov A, Gaestel M (2010). p38 MAP kinase and MAPKAP kinases MK2/3 cooperatively phosphorylate epithelial keratins. J Biol Chem 285, 33242–33251.

Mooseker MS (1985). Organization, chemistry, and assembly of the cytoskeletal apparatus of the intestinal brush border. Annu Rev Cell Biol 1, 209–241.

Oka T, Toyomura T, Honjo K, Wada Y, Futai M (2001). Four subunit a isoforms of Caenorhabditis elegans vacuolar H+-ATPase. Cell-specific expression during development. J Biol Chem 276, 33079–33085.

Omary MB (2009). "IF-pathies": a broad spectrum of intermediate filament-associated diseases. J Clin Invest 119, 1756–1762.

Owens DW, Lane EB (2004). Keratin mutations and intestinal pathology. J Pathol 204, 377–385.

Owens DW, Wilson NJ, Hill AJ, Rugg EL, Porter RM, Hutcheson AM, Quinlan RA, van Heel D, Parkes M, Jewell DP, *et al.* (2004). Human keratin 8 mutations that disturb filament assembly observed in inflammatory bowel disease patients. J Cell Sci 117, 1989–1999.

Pilipiuk J, Lefebvre C, Wiesenfahrt T, Legouis R, Bossinger O (2009). Increased IP3/$Ca^{2+}$signaling compensates depletion of LET-413/DLG-1 in *C. elegans* epithelial junction assembly. Dev Biol 327, 34–47.

Ramms L, Fabris G, Windoffer R, Schwarz N, Springer R, Zhou C, Lazar J, Stiefel S, Hersch N, Schnakenberg U, *et al.* (2013). Keratins as the main component for the mechanical integrity of keratinocytes. Proc Natl Acad Sci USA 110, 18513–18518.

Saegusa K, Sato M, Sato K, Nakajima-Shimada J, Harada A (2014). *Caenorhabditis elegans* chaperonin CCT/TRiC is required for actin and tubulin biogenesis and microvillus formation in intestinal epithelial cells. Mol Biol Cell 25, 3095–3104.

Sarov M, Schneider S, Pozniakovski A, Roguev A, Ernst S, Zhang Y, Hyman AA, Stewart AF (2006). A recombineering pipeline for functional genomics applied to *Caenorhabditis elegans*. Nat Methods 3, 839–844.

Segbert C, Johnson K, Theres C, van Furden D, Bossinger O (2004). Molecular and functional analysis of apical junction formation in the gut epithelium of *Caenorhabditis elegans*. Dev Biol 266, 17–26.

Seltmann K, Fritsch AW, Kas JA, Magin TM (2013). Keratins significantly contribute to cell stiffness and impact invasive behavior. Proc Natl Acad Sci USA 110, 18507–18512.

Stamenovic D, Wang N (2000). Invited review: engineering approaches to cytoskeletal mechanics. J Appl Physiol 89, 2085–2090.

Strnad P, Windoffer R, Leube RE (2001). In vivo detection of cytokeratin filament network breakdown in cells treated with the phosphatase inhibitor okadaic acid. Cell Tissue Res 306, 277–293.

Strnad P, Windoffer R, Leube RE (2002). Induction of rapid and reversible cytokeratin filament network remodeling by inhibition of tyrosine phosphatases. J Cell Sci 115, 4133–4148.

Stutz K, Kaech A, Aebi M, Kunzler M, Hengartner MO (2015). Disruption of the *C. elegans* intestinal brush border by the fungal lectin CCL2 phenocopies dietary lectin toxicity in mammals. PLoS One 10, e0129381.

Tao GZ, Toivola DM, Zhou Q, Strnad P, Xu B, Michie SA, Omary MB (2006). Protein phosphatase-2A associates with and dephosphorylates keratin 8 after hyposmotic stress in a site- and cell-specific manner. J Cell Sci 119, 1425–1432.

Thomas GH (2001). Spectrin: the ghost in the machine. Bioessays 23, 152–160.

Toivola DM, Strnad P, Habtezion A, Omary MB (2010). Intermediate filaments take the heat as stress proteins. Trends Cell Biol 20, 79–91.

van Fürden D, Johnson K, Segbert C, Bossinger O (2004). The *C. elegans* ezrin-radixin-moesin protein ERM-1 is necessary for apical junction remodelling and tubulogenesis in the intestine. Dev Biol 272, 262–276.

Wang L, Srinivasan S, Theiss AL, Merlin D, Sitaraman SV (2007). Interleukin-6 induces keratin expression in intestinal epithelial cells: potential role of keratin-8 in interleukin-6-induced barrier function alterations. J Biol Chem 282, 8219–8227.

Watanabe N, Ishihara T, Ohshima Y (2007). Mutants carrying two sma mutations are super small in the nematode *C. elegans*. Genes Cells 12, 603–609.

Watanabe N, Nagamatsu Y, Gengyo-Ando K, Mitani S, Ohshima Y (2005). Control of body size by SMA-5, a homolog of MAP kinase BMK1/ERK5, in *C. elegans*. Development 132, 3175–3184.

Watanabe S, Punge A, Hollopeter G, Willig KI, Hobson RJ, Davis MW, Hell SW, Jorgensen EM (2011). Protein localization in electron micrographs using fluorescence nanoscopy. Nat Methods 8, 80–84.

Wöll S, Windoffer R, Leube RE (2007). p38 MAPK-dependent shaping of the keratin cytoskeleton in cultured cells. J Cell Biol 177, 795–807.

Woo WM, Goncharov A, Jin Y, Chisholm AD (2004). Intermediate filaments are required for *C. elegans* epidermal elongation. Dev Biol 267, 216–229.

Zhang H, Landmann F, Zahreddine H, Rodriguez D, Koch M, Labouesse M (2011). A tension-induced mechanotransduction pathway promotes epithelial morphogenesis. Nature 471, 99–103.

Zupancic T, Stojan J, Lane EB, Komel R, Bedina-Zavec A, Liovic M (2014). Intestinal cell barrier function in vitro is severely compromised by keratin 8 and 18 mutations identified in patients with inflammatory bowel disease. PLoS One 9, e99398.

# Supplemental Materials

***Molecular Biology of the Cell***

Geisler et al.

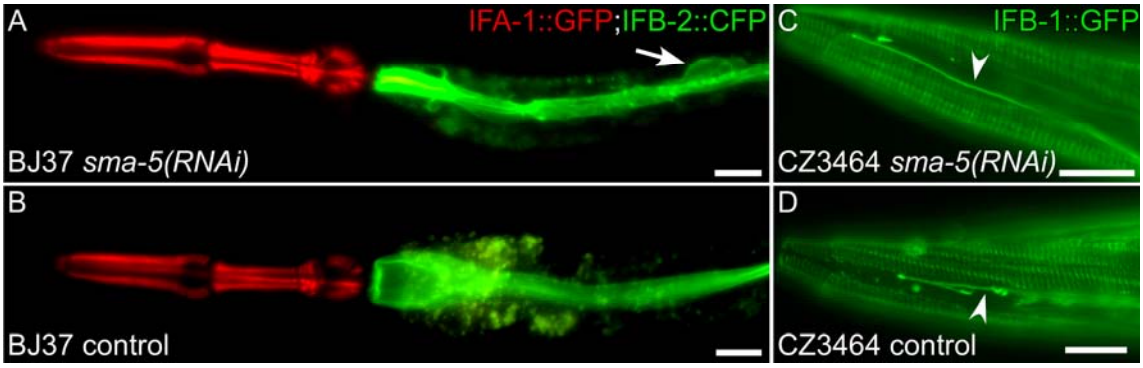


**Figure S1: Down regulation of *sma-5* does not interfere with pharyngeal IFA-1 and hypodermal IFB-1 localization but induces perturbations in IFB-2 distribution of young adult worms.**
*sma-5(RNAi)* in strain BJ37 simultaneously expressing IFA-1::GFP (false red color) and IFB-2::CFP (false green color) does not interfere with the apicobasal bundles of IFA-1::GFP in the pharyngeal marginal cells that are typically found in wild-type worms (B), while IFB-2::CFP is not any more restricted to the subapical domain but surrounds large cytoplasmic invaginations (arrow) protruding from the dilated apical lumen (A). Similarly, *sma-5(RNAi)* does not interfere with the apicobasal distribution of IFB-1::GFP reporters connecting apical and basal hemidesmosomes in the hypodermis of strain CZ3464 (C) compared to control animals (D). Arrowheads in C and D indicate the excretory canal. Scale bars: 20 µm in A-D.

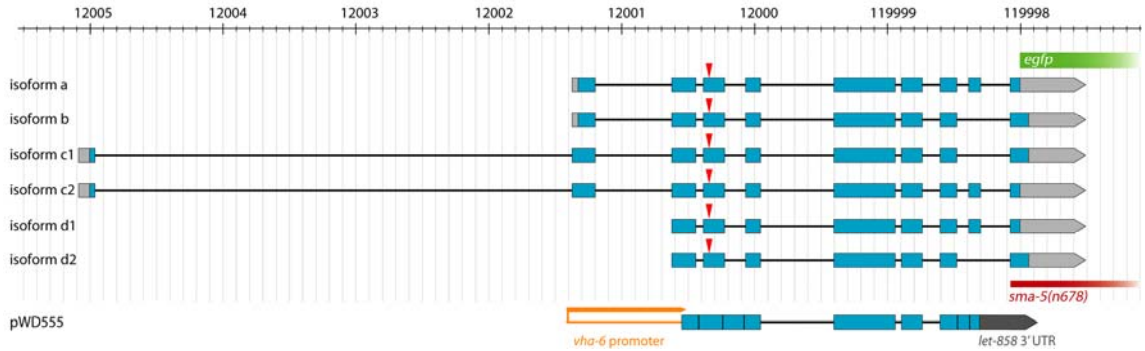


**Figure S2: Multiple SMA-5 isoforms are predicted from the genomic sequence.**
Protein-coding exons are shown in blue, non-coding exons in grey and introns as thin black lines. The predicted variants differ with respect to their amino- and carboxytermini. In addition, alternative splice variants are depicted for isoforms c and d. The position of the point mutation in allele *kc1* is marked by the red arrowhead; the start of the deletion in allele *n678* encompassing the last exon of the *sma-5* gene is also shown. The insertion site of the EGFP-encoding *egfp* cDNA at the 3'-end of the protein-coding sequence in the rescue fosmid is demarcated. Note, that it is joined in frame at the carboxyterminus of isoforms a, c2 and d1 but would result in a small caroboxyterminal deletion in isoforms b, c1 and d2. A cDNA encoding isoform a including three introns was used to prepare the intestine-specific rescue construct *vha-6p::sma-5* (pWD555). The scale bar at the top shows the relative position of the *sma-5* gene fragments on the X-chromosome in units of kb.

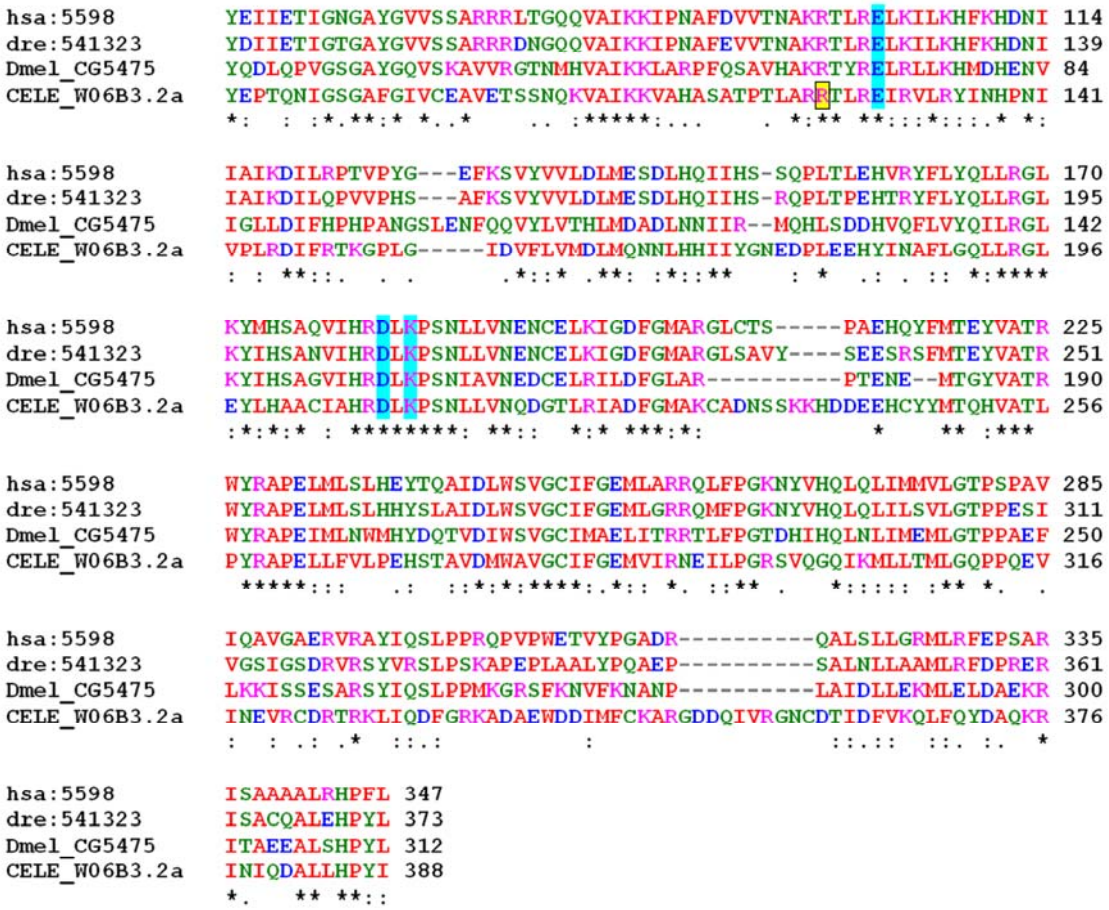


**Figure S3: The predicted catalytic domain of SMA-5 is evolutionary conserved and contains a $R_{125}$->$H_{125}$ mutation in *kc1*.**

A comparison of the predicted catalytic domains of SMA-5 (isoform a; CELE_W06B3.2a) and its orthologs in *Drosophila melanogaster* (Dmel_CG5475), *Danio rerio* (dre:541323) and *Homo sapiens* (hsa:5598) is shown (nomenclature taken from the KEGG database (http://www.genome.jp/kegg)). Asterisks below denote amino acids that are identical and : demarcate conserved amino acids that score > 0.5 in the Gonnet PAM 250 matrix. Amino acid groups are color-coded: blue, acidic; magenta, basic - H; green, hydroxyl + sulfhydryl + amine + G; red; small (small + hydrophobic (including aromatic -Y)). The relative amino acid position is given at the right for the last amino acid in each line. The G→A point mutation in *kc1* at nucleotide position 998 of predicted isoform a (CELE_W06B3.2a) leads to a replacement of conserved $R_{125}$ (yellow, boxed) by $H_{125}$. The mutation is located within the predicted catalytic domain in a highly conserved sequence motif, which shows similarities to *D. melanogaster* (38.5%), *D. rerio* (40.4%) and *H. sapiens* (42.3%) and is adjacent to one of the crucial catalytic and also conserved amino acids (marked in blue).

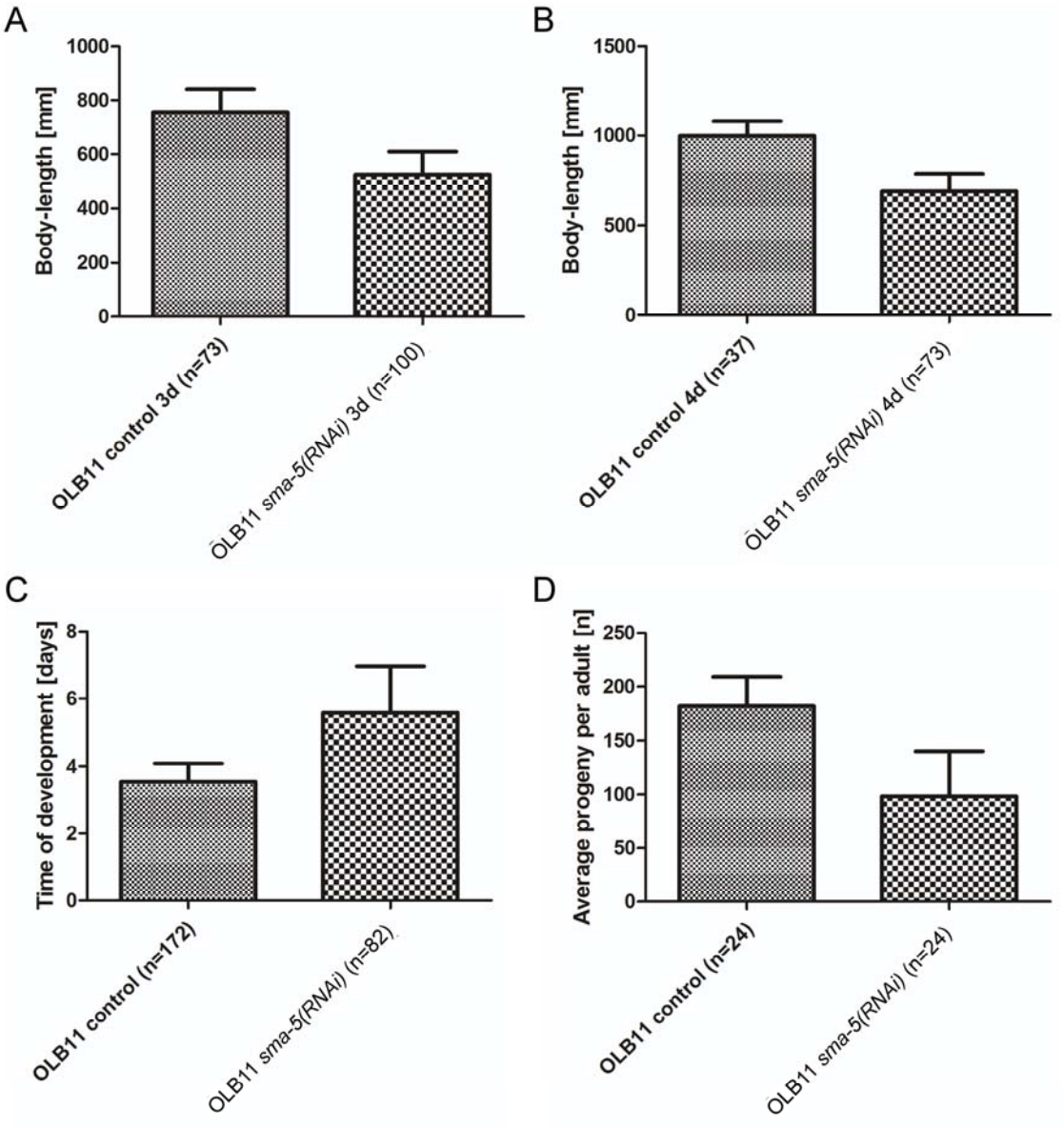


**Figure S4: Intestine-specific downregulation of *sma-5* RNA copies the phenotype of *sma-5(kc1)* and *sma-5(n678)* mutants.**

The histograms show that *sma-5(RNAi)* in strain OLB11 leads to a significantly reduced growth ($p<0.0001$) as measured by reduced body length after 3 days (A; 524.5 ± 8.489 µm [n=100] in treated animals versus 756.2 ± 9.978 µm [n=73] in the wild type) and 4 days (B; 687.7 ± 11.50 µm [n=73] in treated animals versus 998.5 ± 13.50 µm [n=37] in the wild type) of RNAi treatment, significantly increased time of development (C; 5.585 ± 0.152 days; n=82 in treated animals versus 3.547 ± 0.041 days; n=172 in the wild type; $p<0.0001$) and reduced progeny (D; 98.42 ± 14.79; n=24 in treated animals versus 181.8 ± 9.615; n=24 in the wild type; $p<0.001$). For comparison see Fig. 5.

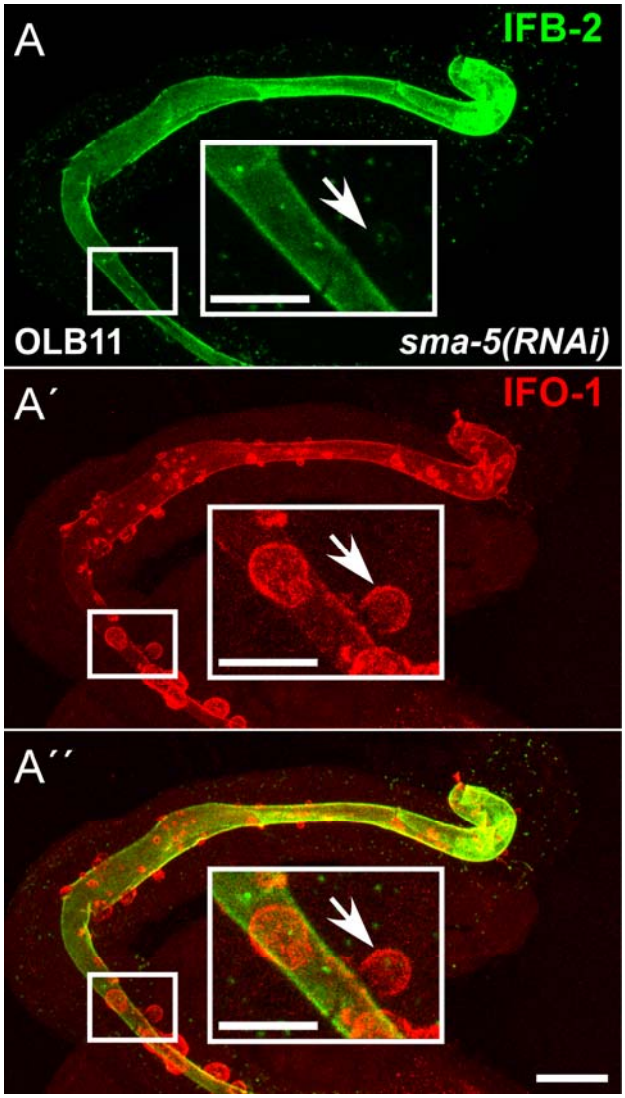


**Figure S5: Some IFO-1-positive invaginations contain little or no IFB-2.**
The fluorescence images show antibody staining of *sma-5(RNAi)*-treated OLB11. Note that some of the IFO-1-positive invaginations lack significant IFB-2 immunolabel (boxed areas; arrow). Scale bars: 10 µm in A-A´´, 5 µm in insets.

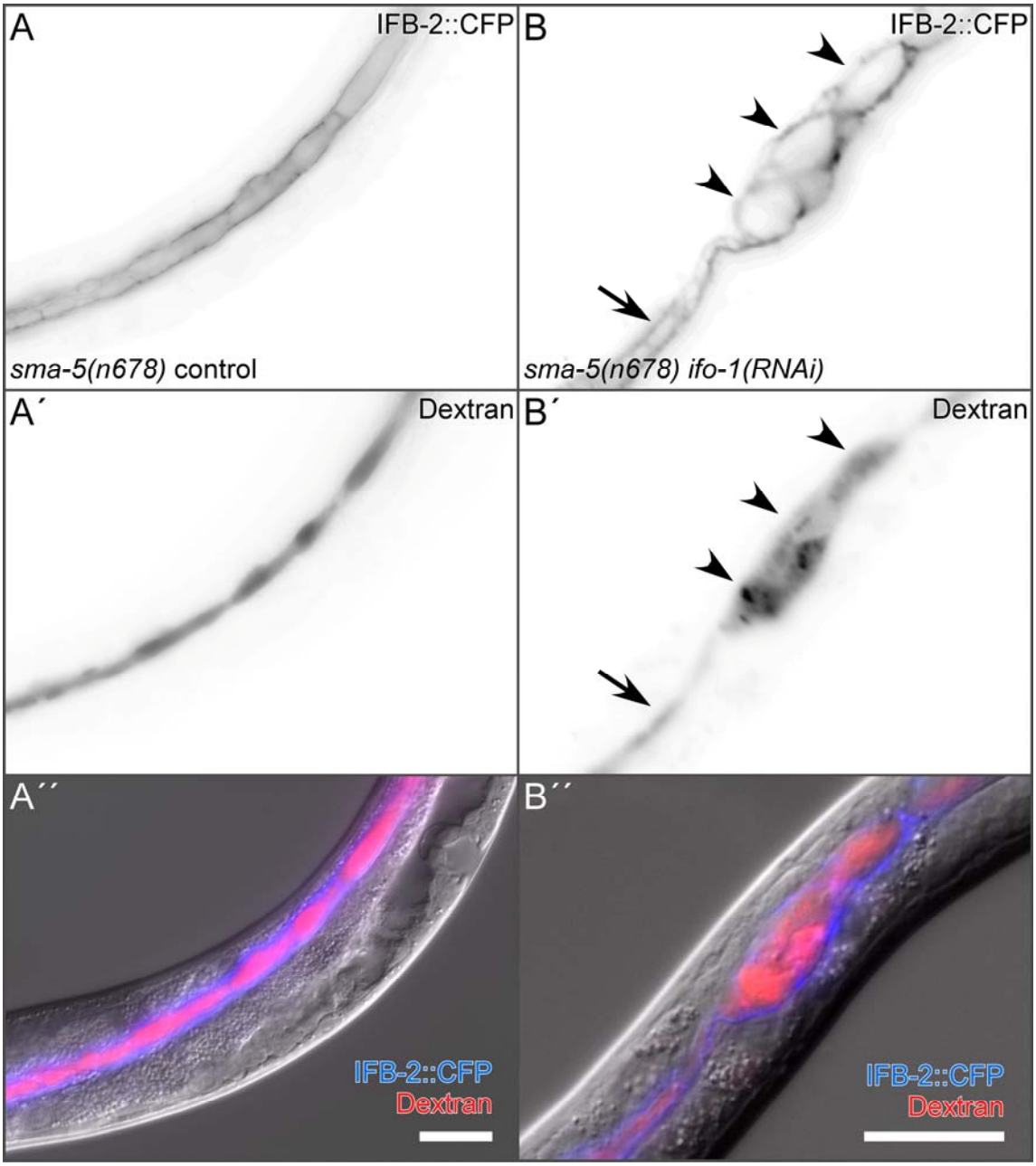


**Figure S6: The *sma-5* and *ifo-1* mutant phenotypes are additive.**
The fluorescence micrographs (inverse presentation) depict the distribution of IFB-2 as assessed by reporter IFB-2::CFP in *sma-5(kc1)* strain BJ132 without (A-A''; n=20) and with *ifo-1(RNAi)* (B-B''; n=10). The worms were fed with Texas Red-dextran for 12 hours prior to imaging. Note that the dextran fluorescence is retained within the IFB-2-lined lumen and cytoplasmic invaginations in both situations (A´´, B´´) demonstrating that the intercellular junctional seal remains intact. The images further show that animals lacking IFO-1 and wild-type SMA-5 present both, IFB-2-positive cytoplasmic invaginations (arrowheads B-B´) typically found in *sma-5* mutants and junctional collapse of IFB-2 (arrows B-B´), which is characteristic for *ifo-1* mutants. Scale bars: 20 µm.

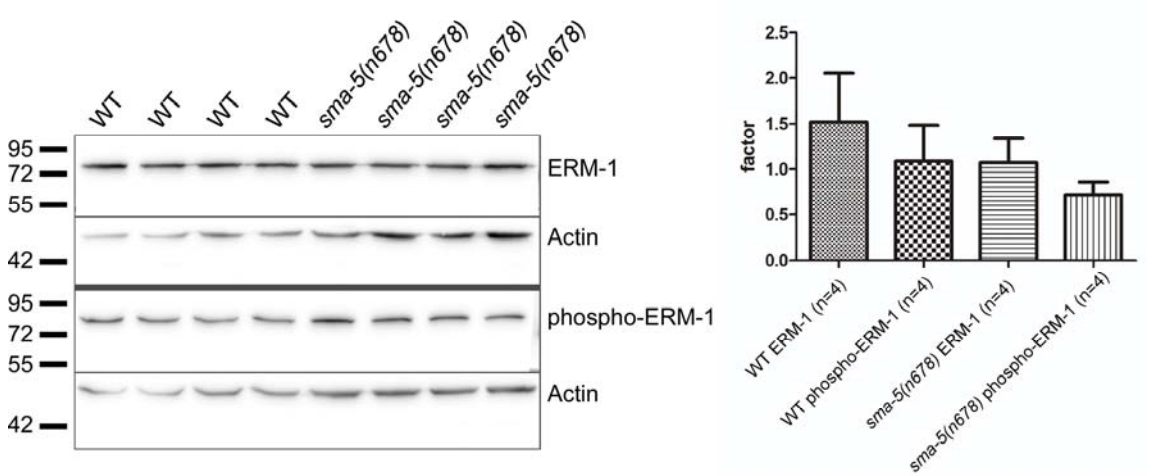


**Figure S7: The level but not the fraction of phosphorylated ERM-1 is reduced in *sma-5(n678)* mutants.**

The immunoblots at left show the reaction of antibodies directed against total ERM-1 (top) and phosphorylated ERM-1 (phospho-ERM-1; bottom) in the wild type (WT) and *sma-5(n678)* mutants. The same blots were stained with actin antibodies for control (lower parts). The position of co-electrophoresed size markers are shown in kDa at left. The results of immunosignal quantification are depicted at right. Note that the overall expression level of ERM-1 is reduced in the mutant background. The fraction of phosphorylated ERM-1, however, remains almost the same (71% in WT versus 67% in *sma-5(n678)*).